life

MDPI

Article

Mineral Indicators of Geologically Recent Past Habitability on Mars

Roger Hart [1,2,*] and Dawn Cardace [2]

[1] Department of Physics and Engineering, Community College of Rhode Island, Lincoln, RI 02865, USA
[2] Department of Geosciences, University of Rhode Island, Kingston, RI 02881, USA; cardace@uri.edu
* Correspondence: rmhart1@ccri.edu

Abstract: We provide new support for habitable microenvironments in the near-subsurface of Mars, hosted in Fe- and Mg-rich rock units, and present a list of minerals that can serve as indicators of specific water–rock reactions in recent geologic paleohabitats for follow-on study. We modeled, using a thermodynamic basis without selective phase suppression, the reactions of published Martian meteorites and Jezero Crater igneous rock compositions and reasonable planetary waters (saline, alkaline waters) using Geochemist's Workbench Ver. 12.0. Solid-phase inputs were meteorite compositions for ALH 77005, Nakhla, and Chassigny, and two rock units from the Mars 2020 Perseverance rover sites, Máaz and Séítah. Six plausible Martian groundwater types [$NaClO_4$, $Mg(ClO_4)_2$, $Ca(ClO_4)_2$, Mg-$Na_2(ClO_4)_2$, Ca-$Na_2(ClO_4)_2$, Mg-$Ca(ClO_4)_2$] and a unique Mars soil-water analog solution (dilute saline solution) named "Rosy Red", related to the Phoenix Lander mission, were the aqueous-phase inputs. Geophysical conditions were tuned to near-subsurface Mars (100 °C or 373.15 K, associated with residual heat from a magmatic system, impact event, or a concentration of radionuclides, and 101.3 kPa, similar to <10 m depth). Mineral products were dominated by phyllosilicates such as serpentine-group minerals in most reaction paths, but differed in some important indicator minerals. Modeled products varied in physicochemical properties (pH, Eh, conductivity), major ion activities, and related gas fugacities, with different ecological implications. The microbial habitability of pore spaces in subsurface groundwater percolation systems was interrogated at equilibrium in a thermodynamic framework, based on Gibbs Free Energy Minimization. Models run with the Chassigny meteorite produced the overall highest H_2 fugacity. Models reliant on the Rosy Red soil-water analog produced the highest sustained CH_4 fugacity (maximum values observed for reactant ALH 77005). In general, Chassigny meteorite protoliths produced the best yield regarding Gibbs Free Energy, from an astrobiological perspective. Occurrences of serpentine and saponite across models are key: these minerals have been observed using CRISM spectral data, and their formation via serpentinization would be consistent with geologically recent-past H_2 and CH_4 production and sustained energy sources for microbial life. We list index minerals to be used as diagnostic for paleo water–rock models that could have supported geologically recent-past microbial activity, and suggest their application as criteria for future astrobiology study-site selections.

Keywords: serpentinization; Mars; astrobiology

Citation: Hart, R.; Cardace, D. Mineral Indicators of Geologically Recent Past Habitability on Mars. *Life* **2023**, *13*, 2349. https://doi.org/10.3390/life13122349

Academic Editors: Jacques Fantini and André Brack

Received: 7 October 2023
Revised: 25 November 2023
Accepted: 5 December 2023
Published: 15 December 2023

1. Introduction

Serpentinization and water–rock reactions on rocky ocean worlds with subsurface silicates interacting with subsurface water layers are increasingly of interest as drivers of planetary habitability [1–7]. Serpentine group minerals have also been detected in the study of asteroids [8], comets [9], and meteorites, especially in some carbonaceous chondrites [10]. Serpentinization relies on available parent minerals in the olivine and pyroxene groups being exposed to water and oxidative alteration through time, producing serpentine minerals and associated phases.

Ultramafic parent rocks produce serpentine-rich alteration assemblages; mafic parent rocks produce albite- and phyllosilicate-rich alteration assemblages, with minor serpentinization. In both cases, rocky solids transform, causing geochemical changes in co-existing aqueous solutions, and may release $H_{2(g)}$ and diverse hydrocarbon-containing compounds over time. Biologically useful hydrogen is produced as Fe^{2+} in olivine is oxidized and H atoms in H_2O are reduced, yielding Fe oxides and free H_2 [10]. H_2 production via low-temperature (30 °C to 70 °C) water–rock reactions has been examined through laboratory studies [11], but are being examined more comprehensively [12].

CH_4 has been identified in both mafic and ultramafic rock units on Earth, predominantly in ophiolites and other settings across various spatiotemporal settings (Supplementary Table S1, references therein, based on [13]). CH_4 and more complex hydrocarbons can be produced from CO_2 and H_2 and through Fischer–Tropsch Type (FTT) synthesis [14–17]. However, FTT reactions cannot be the sole drivers of organic synthesis in planetary materials, given other processes illustrated in the Stecker synthesis, spark discharge experiments, and ultraviolet irradiation studies [18,19].

Examples of reactions of serpentinization resulting in astrobiologically relevant species include reactions presented by Oze and Sharma [20], which include reactions (1)–(3):

$$6Fe_2SiO_4 + 7H_2O = 3Fe_3Si_2O_5(OH)_4 + Fe_3O_4 + H_{2(aq)} \quad (1)$$

$$12FeSiO_3 + 2H_2O + CO_{2\,(aq)} = 4Fe_3O_4 + CH_4 + 12SiO_{2(aq)} \quad (2)$$

$$12FeSiO_3 + 2H_2O + CO_{2\,(aq)} = 4Fe_3O_4 + CH_4 + 12SiO_{2[\text{Amorphous Silica}]} \quad (3)$$

Key gas-phase reactions associated with these processes are shown in reactions (4) and (5):

$$4H_2 + CO_2 = CH_4 + 2H_2O \quad (4)$$

$$H_2 + SO_2 = H_2S + O_2 \quad (5)$$

Subsurface mafic–ultramafic rock alteration processes arguably produce H_2 and CH_4 over long time periods, and provide sheltered niches for life, like porous voids, and the preservation of biosignatures. At the same time, mafic and ultramafic rocks on Mars are well- constrained from the meteorite record [21–26] and recent rover reports from Jezero Crater sites [27–29]. Further, plausible paleo groundwater chemistries for Mars have been rigorously vetted [30–43]. Diverse alteration products of water–rock reactions have been documented on Mars [26,44–53]. Alteration minerals record environmental change and geochemical transitions, serving as proxy data for changing (geologically controlled) habitability [51,54–57].

Increasingly well-resolved surface mineralogy data for Mars (buttressed by rover-derived data streams) provide an excellent basis for models of water–rock interactions. For example, olivine- and pyroxene-bearing material has been mapped in the Nili Fossae region [58,59]. In this ~30,000 km^2 region on Mars, a large depression has been described as mélange terrain (elevation −0.6 km, Syrtis Major quadrangle, ~22° N, ~75° E) [46]. Olivine in the Nili Fossae protolith ranges compositionally from 30 to 70% fayalite (Fe_2SiO_4, [47]); prior work identified surface olivine and a generally basaltic composition [48]. Higher percentages of fayalite produce stoichiometrically more molecular hydrogen via serpentinization-driven reactions, for example reaction (1). Complementary investigations targeting Nili Fossae olivine using the OMEGA spectrometer on Mars Express [60,61] identified adjacent phyllosilicate deposits [44,62], and serpentine has been confirmed [46,50,63–65]. Spatially related smectite, carbonate and serpentine found in this area likely correspond to discrete alteration events [66].

Presently, the Mars 2020 Perseverance rover is collecting data near its Jezero Crater landing site, seeking signs of past life [67–70]. Prior scientific work assessed the astrobiological potential of ancient Mars, surface geological properties and processes, and Martian habitability [71–76]. Recent discoveries by the Perseverance rover during the Mars 2020

mission have characterized two basement igneous rock units, one mafic unit (Máaz) and a deeper ultramafic unit (Séítah), which show evidence of aqueous alteration [27]; spectral data for the Séítah unit suggest talc or serpentine [77] This Noachian-aged basin [78] likely experienced aqueous alteration between 3.8 and 3.2 Ga [78–80], possibly as a lake-like system [80–82]. We aim to provide a theoretical model of possible mineralogy, associated with plausible habitability for a better targeting of further exploration of the Martain surface and near-subsurface.

Mindful of sustained interest in assessing the habitability of the Martian near-subsurface and future mineralogical datasets for material sampled by Perseverance, we model the reactions of three Martian meteorites and the Máaz and Séítah lithologies with plausible Martian waters. In this work, we examine the geochemical evolution of plausible subsurface pore- and/or fracture-network environments, which conceptually correspond to Nili Fossae rock units located proximal to the Jezero Crater. Modeling inputs (rock and water types) are well supported by existing data, and modeling outputs (secondary minerals and altered waters/evolved gases) are thoughtfully compared to modern observations. Surveying the products of water–rock alteration models, we isolate mineral tracers of specific geologically recent paleo water–rock interactions.

Further, we assess the spontaneity of four common microbial metabolic reactions in Mars-relevant mafic–ultramafic systems, to determine which mineral indicators correspond to specific paleo habitats on Mars. Diagnostic secondary minerals for specific water–rock reaction paths ranged from singular phases to unique sets of minerals. Most simply, a single diagnostic phase is keyed to a reaction path model; the mineral saponite-Na is related uniquely to the Séítah reactions in the Rosy Red simulated fluid. A specific set of minerals defines the Séítah reactions with the $NaClO_4$ type of water: key products are natrolite with phlogopite. In other cases, more minerals constitute the diagnostic sets that correspond to specific water–rock reaction paths. In all, we provide new model results that underscore the importance of the co-occurrence of serpentine and saponite as indicator minerals in remotely sensed or rover-based data streams, as signaling promising sites for astrobiological investigation.

2. Materials and Methods

We modeled aqueous alteration of mafic and ultramafic rocks using The Geochemist's Workbench (www.gwb.com (1 December 2023)), 12th Edition, without selective phase suppression, to determine solid–liquid–gas–phase equilibrium species [83] in the near-subsurface on Mars.

2.1. Water–Rock Geochemical Modeling

2.1.1. Code and Database

Solute activity was calculated using the extended Debye–Hückel B-dot equation, useful for ionic strengths of up to 3 molal solutions, from 273 K to 573 K [83–85]. We used the Geochemist's Workbench modeling platform, to extend prior water–rock modeling in planetary contexts [3–7,66,86–94]. The extended Debye–Hückel B-dot equation was engaged, since all modeled ionic strengths considered here are between 0.0407 and 3.435 molal at $\xi = 1$. Eh ranges for all simulations are between −893.0 and −208.0 mV, is reducing, and generally similar to, some terrestrial groundwaters, high-salinity waters, or water–rock systems isolated from our oxygen-rich atmosphere.

We utilized the thermodynamic database from thermo.com.V8.R6+.tdat, distributed at https://www.gwb.com/data/thermo.com.V8.R6+.tdat (1 December 2023) [95]. Temperatures were held constant, modeled at 373.15 K, simulating recent-geologic-past magmatic-, impactor-, or radionuclide-derived heat sources (e.g., small-to-medium craters ~20–30 km in diameter produce a range of ~373 to 393 K [96] or radionuclides [2,4]). Pressure was constant at 1.013 kPa. Generally, water/rock ratios were ~1:1 kg, with the addition of solutes increasing the mass of the water slightly; this is a relatively low water–rock ratio,

hypothesized to have occurred in subsurface or lacustrine environments in the geologically recent past [41,97–102].

Limitations exist in every modeling simulation. We recognize that model inputs are bulk rock representations, lacking fine-scale mineralogy or mineral chemistry; as such, the models are more broadly applicable to mafic–ultramafic-hosted systems. We assume that the reactant water aptly represents the recent-geological-past natural waters on Mars/in Martian meteorites, leveraging the critical works of Toner et al. [103–105] and Leong and Shock [13], to validate this choice. We applied an equilibrium modeling approach, reacting all available reagents, in an effort to consider the changing distribution of phases as equilibrium is approached; in nature, a flow-through system could replenish limiting reagents (e.g., through diffusion or advection). Also, we would state that the thermodynamic database used in this work did not account for all mineral solid solutions across all compositions [7,83].

Modeling experiments are always fundamentally constrained by the boundaries of the selected thermodynamic database, which establishes the mineral phases to be considered in any derivative model. We did not deliberately suppress any phases, and share all model outputs. We carefully interpret reaction-path-modeling outputs by evaluating minerals not likely to form in terrestrial-planet geological conditions, based on conventional geological principles, and consider the broader impacts of the chemical inventory of the system, to safeguard the applicability of the results.

2.1.2. Geophysical Considerations

The modeled environment is appropriate for depths greater than ~5 m below the surface of Mars, at low latitudes. The Nili Fossae experience a Martian equatorial climate [106], and temperatures measured by the Thermal Emission Imaging System (THEMIS) are between ~250 and 300 K [59]. This is in the range of the freezing point of a 3–5% saltwater solution with density of ~1035 kg/m^3 [36,38,39,43,84,103]. In addition, the subsurface mafic–ultramafic rock unit at the Nili Fossae (taken at ~9 m′ depth) has enough radiation shielding to allow life; at this depth, cells and biological debris would be beyond the incident electromagnetic and energized-particle irradiated zone, which would ionize biological molecules and render the environment sterilized [107,108]. The current depth of this sterilization is estimated at 2 to 4 m′ depth beneath the Martian regolith, depending on the density of the overlying material; the maximum depth depends on assumptions regarding near-surface Martian soil properties and a deeper mafic–ultramafic unit [108]. We model water-rock reactions at temperatures and pressures relevant to these clement subsurface horizons, as putative habitats.

2.1.3. Input Conditions in Modeling: Solids

Observed rock-forming silicates on Mars and associated weathering products are consistent with model inputs. Primary olivines have been detected on Mars [28,58,60,109–117], as have clinopyroxenes [60,116].

The olivine-rich surface layer observed at the Nili Fossae on Mars overlays a phyllosilicate basement [60,77,109–111,118]; basement rocks were likely severely fractured by ancient impacts, with possible extensive alteration. This region is proximal to the altered, basaltic rocks of the Máaz formation, which exhibits FeO values of ~20 wt %, and the high-olivine ultramafic rock unit, with FeO values of ~30 wt % [28].

Perseverance rover-based data for two sites on the Martian surface are used to structure two specific reaction paths. Mineralogical evaluation of the Máaz site by Farley et al. [27] suggests the presence of augite, plagioclase, ilmenite, ferrosilite, and unidentified iron oxide solids. Materials observed at the Séítah site on Mars show the presence of olivine, augite with minor feldspars, phosphates, and Cr- and Ti-bearing Fe oxide solids [27].

Regarding the meteorite record, SNC meteorites are classified as mafic-to-ultramafic rocks of Amazonian age, between ~3.0 Ga, and the present [119–126]. Major SNC meteorite minerals resemble terrestrial mafic igneous rock compositions (olivine, plagioclase,

clinopyroxene, and orthopyroxene [126]). Minor minerals include shock glasses, Cr-spinel, sulfide minerals, phosphates, titanomagnetite, ilmenite, zircon and silica minerals [126].

Martian meteorites (shergottites, nakhlites, and chassignites, together known as 'SNC meteorites'), are rare samples of Mars's minerals, geochemical inventories, and petrological textures. SNC meteorites are essentially samples of the Martian crust or mantle ([126]; references therein), and are investigated with respect to volcanic processes, the alteration, structural and stratigraphic analysis of igneous processes, the volatile content of the subsurface, and impact event processes. With the return of samples from the Mars 2020 Perseverance mission, unparalleled mineralogical and geochemical analyses are possible for target Martian rocks with specific locality information [74]. These meteorite groups have also had extensive associated geochemical modeling (e.g., [6,86,87,89,127–130]) to which this work can be compared.

Here, data for the Máaz and Séítah research sites, as well as for selected meteorite types, were input as average whole-rock compositions (Figure 1). Input data are provided in Figure 1 and Supplementary Table S2 for ALH77005 (lherzolitic shergottite), Chassigny (chassignite type), and Nakhla (nakhlite type), all from Lodders [21] and the Perseverance rover research sites, Máaz and Séítah (as reported in [27]).

2.1.4. Input Conditions in Modeling: Fluids

Martian groundwater inputs derive from Toner et al. [103], informed by other significant works [37,42,131,132], incorporating (i) the detection of chlorate during the Mars polar Phoenix mission [36,133,134] and (ii) possible evidence of subglacial water at the Martian pole via Mars Express spacecraft radar evidence [135]. Martian groundwater studies [40,42,136] and the premise that modern Mars may exhibit a perchlorate-type water that has high levels of salinity [43,103,137,138] influenced water chemistry inputs in this work. Taken together, even in the harsh, modern Martian environment, it is possible that subsurface waters could support biological processes [137–140]. Microscopic-scale subzero water in chemical reactions like peroxide decomposition and sulfate formation, not considered here, is important for astrobiology [30].

Initial water compositions were generally characterized by the following chemistry: $NaClO_4$, $Mg(ClO_4)_2$, $Ca(ClO_4)_2$, Mg-$Na_2(ClO_4)_2$, Ca-$Na_2(ClO_4)_2$, and Mg-$Ca(ClO_4)_2$ [105]; these waters have perchlorate as the dominant anion and have freezing-point depression properties [30,104,137]. Salts expected to occur in regolith materials have been identified on Mars (cf. [33,38,141]. In parallel, a soil-water analog solution based on digestion of Mars regolith from Rosy Red, a Phoenix Lander site [103], served as another input ("Rosy Red"). All were considered under present-day Martian atmospheric properties [142] (comprehensive list of properties in Supplementary Table S3).

2.2. Statistical Analysis of Modeled Results

Statistical discrimination of relationships in model outputs focused on equilibrium mineral assemblages, since minerals outlast aqueous or gas phases. We utilized the statistical analysis program JMP®, Version Pro 16. SAS Institute Inc., Cary, NC, USA, 1989–2023, applying robust multivariate principal component analysis (RPCA) to cleaned data [136,143–145]. Statistical treatment was based on data covariances [145–147]. Eigen decomposition was applied to the covariance matrix to determine the eigenvalues of the modeled dataset, and allow its interpretation [146,147].

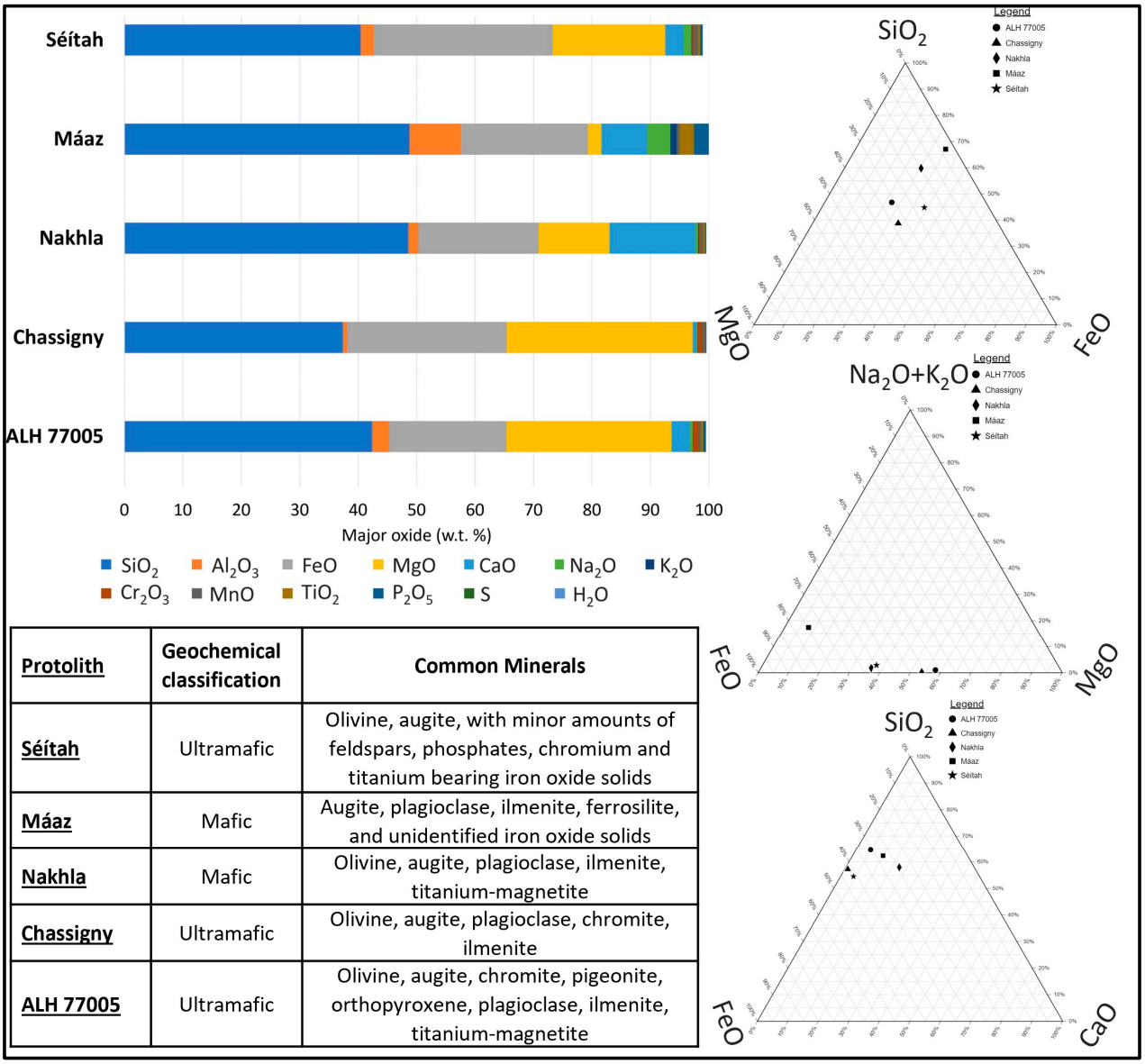

Protolith	Geochemical classification	Common Minerals
Séítah	Ultramafic	Olivine, augite, with minor amounts of feldspars, phosphates, chromium and titanium bearing iron oxide solids
Máaz	Mafic	Augite, plagioclase, ilmenite, ferrosilite, and unidentified iron oxide solids
Nakhla	Mafic	Olivine, augite, plagioclase, ilmenite, titanium-magnetite
Chassigny	Ultramafic	Olivine, augite, plagioclase, chromite, ilmenite
ALH 77005	Ultramafic	Olivine, augite, chromite, pigeonite, orthopyroxene, plagioclase, ilmenite, titanium-magnetite

Figure 1. Initial protolith inputs for reaction path modeling showing their major oxide w.t. % of ALH77005 (lherzolitic shergottite, Chassigny (Chassignite type), Nakhla (Nakhlite type)), Perseverance sites, Máaz and Séíta, and three common ternary plots, SiO_2-MgO-FeO on top, Na_2O+K_2O-FeO-MgO in the middle, and SiO_2-FeO-CaO on the bottom. Chassigny, Séítah, and ALH77005 all exhibit between 48 and 59 w.t. % FeO+MgO values, and are considered ultramafic. Nakhla and Máaz are considered mafic. Nakhla shows an approximate FeO+MgO value of 33%, and Máaz a value of ~24%. (Supplementary Figure S1 displays how PC1 is largely controlled by MgO (approx. −0.85, SiO_2 (approx. 0.34), and CaO (approx. 0.31), and PC2 is largely controlled by FeO (approx. −0.65), CaO (approx. 0.51), and MgO (approx. 0.36)). Note that the subset table shows protolith geochemical classifications and major minerals, as reported for the meteorites [21] and the two Perseverance sites [27].

2.3. Bioenergetic Computations

Bioenergetic modeling (as in [148–151]) quantifies Gibbs Free Energy (ΔG_r) values for reactions of interest. ΔG_r is the sum of the standard-state Gibbs Free Energy value (ΔG_r^o) at the conditions of interest (373.15 K, associated with residual heat from an impact event or magmatic system, and 101.3 kPa, similar to <10 m depth), and the product of the gas

constant (R), temperature (T, in Kelvin), and the natural log of the activity product (Q_r), as in Equation (6):

$$\left(\frac{\Delta Gr}{d\xi}\right) = \Delta G_r^o + RT\ lnQ_r\ . \quad (6)$$

The activity product, Q_r, was computed using the activity data for ith species, a_i, and $v_{i,r}$, the stoichiometric reaction coefficient of the ith species, as in Expression (7):

$$Q_{,r} = \prod a_i^{v_{i,r}} \quad (7)$$

When ΔG_r is negative, by convention, the modeled reaction is thermodynamically favorable; we infer a feasible microbial metabolic reaction, or a habitable niche. When the system is at constant temperature and pressure, ΔG_r varies with the extent of the chemical reaction (ξ), as the activities of relevant species shift. Activity data from GWB output files were used in calculations (Supplementary Table S3).

Four generalized microbial metabolic reactions were targeted in this study, as in previous work [150–156]. The Gibbs Free Energy computation values for each reaction (kJ/mol) were normalized to the number of electrons (e^-) transferred [156]. These reactions are known to support microbial activity in Earth environments, and represent key carbon transformations that may be important for Martian settings:

$$\text{sulfate reduction } [SO_4^{2-} + 4H_{2(aq)} + 2H^+ = H_2S_{(aq)} + 4H_2O_{(l)}]; \quad (8)$$

$$\text{methanotrophy } [CH_{4(aq)} + SO_4^{2-} + H^+ = HCO_3^- + H_2S_{(aq)} + H_2O_{(l)}]; \quad (9)$$

$$\text{methanogenesis } [CO_{2(aq)} + 4H_{2(aq)} = CH_{4(aq)} + 2H_2O_{(l)}]; \text{ and} \quad (10)$$

$$\text{anaerobic methane oxidation, or AMO } [SO_4^{2-} + 2H^+ + CH_{4(aq)} = CO_{2(aq)} + H_2S_{(aq)} + 2H_2O_{(l)}] \quad (11)$$

3. Results

3.1. Bulk-System Geochemistry

We modeled the reactions of the five protoliths with seven plausible planetary waters, resulting in different equilibrium solid, aqueous, and gas assemblages. Inputs are provided in Supplementary File S1. Our results show that (i) modeled solid products reproduce many minerals known to be part of Martian (near-)surface materials, and (ii) some modeled product waters have higher total dissolved solids than are typically observed in terrestrial serpentinites, while pH values are within the range of continental serpentinization systems, such as in Oman, Coast Range, Del Puerto, and Bay of Islands Ophiolites (Supplementary Table S1).

Water and protolith chemistries exert important controls on serpentinization-related reaction products (Figure 2). For example, in all 373 K models, modeled reaction paths drive pH variation. Starting solutions (ξ = 0) were all acidic, ranging from pH ~ 5.04 to 5.286; equilibrium solutions (ξ = 1) were mostly basic, except for two simulations that retained acidic pH values. Recall that the pH of neutrality at 373 K is 6.13, not 7. The Máaz reaction path with $Mg(ClO_4)_2$ water yielded a final solution pH of 5.27 (acidic), and the Máaz reaction path with $CaMg(ClO_4)_2$ water yielded a final solution pH of 5.39 (acidic). For comparison, the Chassigny reaction path with $CaMg(ClO_4)_2$ water resulted in a final solution pH of 6.4 (basic), and Chassigny reacted with $Na_2Mg(ClO_4)_2$ water resulted in a final solution pH of 6.6 (basic); Nakhla reacted with $Mg(ClO_4)_2$ water resulted in a final solution pH of 6.7 (basic). The more corrosive (acidic) solutions were generated by the Máaz-based models.

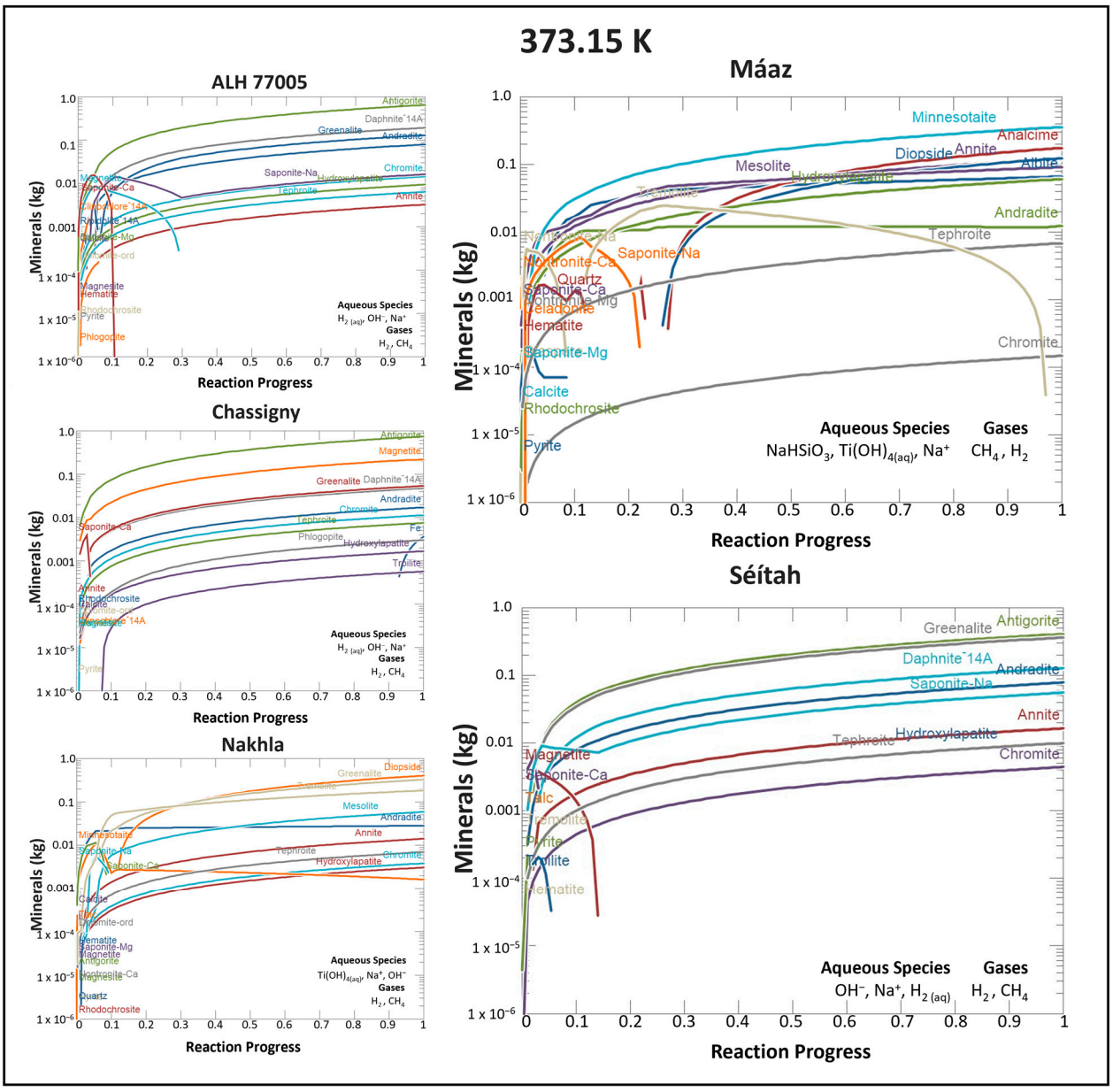

Figure 2. Representative charts of reactions with the modified Rosy Red Mars Phoenix Lander simulant water. Meteorite protoliths (ALH77005, Chassigny, and Nakhla) and Mars 2020 Perseverance rover sites (Máaz and Séítah) reacted at 373.15 K. All plots show the major minerals produced (kg) on the vertical axis; inset text shows dominant species at equilibrium in aqueous and gas phases. Equilibrium minerals, waters, and gases differ. Specifically, Máaz yields a minnesotaite–mesolite-annite assemblage (pyrophyllite- and mica-bearing, with zeolites) and Séítah models yield an antigorite–greenalite–daphnite–andradite assemblage (dominated by serpentine, chlorite, and hydrogarnet groups). Further, the expected aqueous Cl^- and $H_{2(aq)}$ values diverge, and H_2:CH_4 ratios vary between models (see supplementary documents for specific values).

The dominant product mineral by mass (>100 g formed) in many models was the mineral antigorite (a serpentine, general composition $Mg_3Si_2O_5(OH)_4$ [147]). Responding to temperature, system chemistry, and oxygen fugacity (fO_2), other important product minerals included iron-rich oxides (hematite, magnetite) and other phyllosilicates (greenalite (a mixed-valence state Fe-serpentine), cronstedtite (a mixed-valence state Fe-serpentine, with some Fe substitution for Si), saponite (calcium-rich trioctahedral smectite), daphnite (magnesian chamosite, a chlorite mineral), and andannite (Fe-rich biotite)). Hydroxylap-

atite (OH-apatite, a phosphate mineral, and andradite (garnet group, often hydrated in model outputs) were repeatedly observed.

Several solid phases were predicted by the thermodynamic modeling, but are not likely to be stably produced at 373 K (100 °C) in quasi-diagenetic alteration conditions. These phases are either pure metallic solids such as "$Fe_{(s)}$" or rock-forming primary minerals, including "FeO" (an ideal ferrous iron oxide, not necessarily the mineral wüstite), "tremolite" (amphibole group, a Ca- Mg-silicate), "diopside" and "hedenbergite" (clinopyroxene endmember minerals, Ca- Mg- Fe-silicates with variable cation substitution), "tephroite" (Mn-silicate), and "chromite" (an Fe- Cr-oxide mineral, in the spinel group). These modeled product phases should be considered as chemical placeholders, showing that an equilibrium-phase assemblage, which includes, for example, a diopside, would necessarily (stoichiometrically) use up the available Ca, Mg, Fe, Mn, Cr, Si, and O in the system. Diverse phyllosilicates and metastable mineral intermediaries are possible, though not in the selected thermodynamic database, and thus not queried by our model. Tremolite, for example, has not been empirically observed as a secondary phase.

Common terrestrial secondary minerals in mafic rock weathering (largely phyllosilicates) and zeolite or seafloor diagenetic minerals are eminently reasonable model outputs. Other solid phases that repeat in model outputs, but that often occur in higher temperature/magmatic systems found on Earth, include (hydroxyl)apatite, hydrogarnets, troilite, annite, and quartz; these phases, though less common, are supported in the diagenetic literature, and are regarded also as valid model results.

Important aqueous products include Cl^-, Na^+, Ca^{2+}, $H_{2(aq)}$, Mg^{2+}, $CH_{4(aq)}$, HCO_3^- and $CO_3^{2-}{}_{(aq)}$, $SO_4^{2-}{}_{(aq)}$. Dominant gases produced in these simulations were $H_{2(g)}$ and $CH_{4(g)}$, with minor $H_2O_{(g)}$.

3.1.1. Key Mineral Products: Martian Meteorite-Based Models

Modeling based on the three meteorite reactants yielded differing results. The phyllosilicate minerals greenalite and daphnite were produced in abundances greater than 0.25 moles (at ξ = 1) for models with ALH 77005, Nakhla, and Chassigny. Minor minerals produced in each reaction path differed from model to model (see Supplementary File S1).

Reaction paths with ALH77005 commonly produced antigorite (~0.159 to 0.172 moles), daphnite-14Å (~0.298 to ~0.309 moles), and greenalite (~0.358 to ~0.445 moles). To lesser extents, "chromite" (~0.068 to ~0.071 moles) and hydroxylapatite (~0.064 to ~0.071 moles) were also produced in all models. Andradite garnet (~0.057 to ~0.178 moles) and "tephroite" (~0.033 to ~0.0035 moles) were produced in all reaction paths except with $Mg(ClO_4)_2$-type water. Troilite was produced in all reaction paths except with $NaClO_4$-type water. Annite was only produced in the $NaClO_4$ and Rosy Red models. "Diopside" (~0.068) was produced in only the $Ca(ClO_4)_2$ and $CaNa_2(ClO_4)_2$ models. Magnetite (~0.006 to ~0.02) was produced in the $CaMg(ClO_4)_2$, $Mg(ClO_4)_2$ and $Na_2Mg(ClO_4)_2$ models. Saponite was only produced in the $NaClO_4$ model.

All reaction paths with Chassigny yielded the silicate minerals antigorite (~0.164 to ~0.183 moles), daphnite-14Å (~0.066 to ~0.077 moles), hydroxylapatite (~0.0033 to ~0.0037 moles), and greenalite (~0.142 to ~0.191 moles). Oxide minerals such as "chromite" (~0.048 to ~0.056 moles) and magnetite (~0.83 and ~1.01 moles) were produced, along with additional "elemental Fe" (~0.29 to ~0.43 moles). Andradite garnet (~0.033 to ~0.045 moles) was produced in the $Ca(ClO_4)_2$, $CaNa_2(ClO_4)_2$, $NaClO_4$, and Rosy Red models, and phlogopite (~0.0072 to ~0.0086 moles) was produced in $NaClO_4$ and Rosy Red models. Troilite (~0.0064 to ~0.089 moles) was produced in all cases. "Tephroite" (~0.037 to ~0.041 moles) was produced in $Ca(ClO_4)_2$, $CaNa_2(ClO_4)_2$, $NaClO_4$, and Rosy Red models.

In the Nakhla reaction paths, "diopside" was the dominant mineral produced, in terms of mass. Other minerals included andradite (~0.022 to ~0.035 moles), annite (~0.027 to ~0.031 moles), hydroxylapatite (~0.0060 to ~0.0067 moles), greenalite (~0.886 to ~1.009 moles), and chromite (~0.017 to ~0.019 moles). "Tremolite" was produced in all reactions (~0.198 to ~0.684 moles) except Rosy Red. "Diopside" (~1.48 to ~2.30 moles) and mesolite (~0.151 to

~0.167 moles) were produced in all models except the $Mg(ClO_4)_2$ model. The $Ca(ClO_4)_2$ and Rosy Red reactions produced minnesotaite (~0.0005 to ~0.005 moles). Antigorite (~0.039 moles) and magnetite (~0.032 moles) were only produced in the $Mg(ClO_4)_2$ reaction. Prehnite was only produced in the $Ca(ClO_4)_2$ reaction (~0.014 moles). Saponite-Ca was only produced in the $Mg(ClO_4)_2$ reaction (~0.199 moles) and Saponite-Na was only produced in the $NaClO_4$ reaction (~0.015 moles).

3.1.2. Key Mineral Products: Jezero Crater Protolith Models

Water–rock models based on Máaz and Séítah rock unit inputs yielded markedly different results. Figure 3 shows that minerals produced in abundances greater than 0.25 moles (at ξ = 1) were common to most models; minnesotaite (a pyrophyllite-talc group mineral), "diopside", mesolite, and quartz were common. Antigorite and greenalite (two serpentines) were absent from Máaz models, but present in Séítah models. Minnesotaite was absent from Séítah model products.

In the Máaz models, minnesotaite was the dominant mineral produced, in terms of mass. At equilibrium, the minerals minnesotaite (~0.741 to ~1.06 moles), mesolite (~0.21 to ~0.877 moles), "chromite" (~0.066 to ~0.073 moles) and hydroxylapatite (~0.116 to ~0.133 moles) were produced in all simulations. Annite (~0.154 to ~0.263 moles) and andradite (~0.0079 to ~0.044 moles) were present in all simulations, except in the $CaMg(ClO_4)_2$ case. "Tephroite" was present (~0.033 to ~0.036 moles), except in the $CaMg(ClO_4)_2$ model; annite was produced, except in the $CaMg(ClO_4)_2$ case. Quartz (~0.421 to ~1.44 moles) was produced in all simulations except the Rosy Red and $NaClO_4$. "Diopside" (~0.479 to ~0.631 moles) was produced in all models except $CaMg(ClO_4)_2$ and $MgNa_2(ClO_4)_2$. "Tremolite" (~0.017 to 0.176 moles) was produced in only the $MgNa_2(ClO_4)_2$ and Rosy Red models. Saponite-Na (~0.024 moles) was produced only in the $MgNa_2(ClO_4)_2$ models. Pyrite (~0.00011 to ~0.005 mole) was produced in the $CaMg(ClO_4)_2$ and $MgNa_2(ClO_4)_2$ models. Alabandite (~0.0007 to ~0.00098 mole), a rare Mn-sulfide mineral, was produced in the $Ca(ClO_4)_2$, $CaNa_2(ClO_4)_2$, and $Mg(ClO_4)_2$ reaction simulations. Albite (~0.158 to ~0.281 moles) was produced in $MgNa_2(ClO_4)_2$, $NaClO_4$, and Rosy Red simulations. Nontronite-Na (~0.0039 mole) was produced only in the $CaMg(ClO_4)_2$ case. Saponite-Na (~0.024 moles) was only present in the $MgNa_2(ClO_4)_2$ case. Saponite-mg (~0.295 moles), muscovite (0.210 moles), and diaspore (~0.317 moles) were produced only in the $CaMg(ClO_4)_2$ case. "Hedenbergite" (~0.079 to ~0.081 moles) was only present in the $Ca(ClO_4)_2$, $CaNa_2(ClO_4)_2$, and $Mg(ClO_4)_2$ cases.

The Séítah simulations yielded greenalite as the mineral in the highest molar abundances (~0.980 to 1.207 moles). In all models, andradite, antigorite, "chromite", daphnite-14Å, greenalite, hydroxylapatite, and "tephroite" are produced. Molar distributions were: andradite (~0.06 to ~0.179 moles); antigorite (~0.104 to ~0.111 moles); "chromite" (~0.020 to ~0.022 moles); daphnite-14Å (~0.150 to ~0.238 moles); hydroxylapatite (~0.020 to ~0.022 moles); and "tephroite" (~0.051 to ~0.055 moles). Other minerals were commonly produced in Séítah models, but in different proportions. Annite populated nearly all model outputs (~0.010 to ~0.027 mole), but was absent in the $NaClO_4$ case. Troilite (~0.001 mole) and "diopside" (~0.119 to ~0.224 moles) were produced in all models except the $NaClO_4$ and the Rosy Red cases. Some minerals were only produced in one simulation for the Séítah models: natrolite (~0.076 moles) was only produced in the $NaClO_4$ case, phlogopite was produced in the $NaClO_4$ models (~0.036 moles), and saponite-Na (~0.145 moles) was produced in only the Rosy Red simulations.

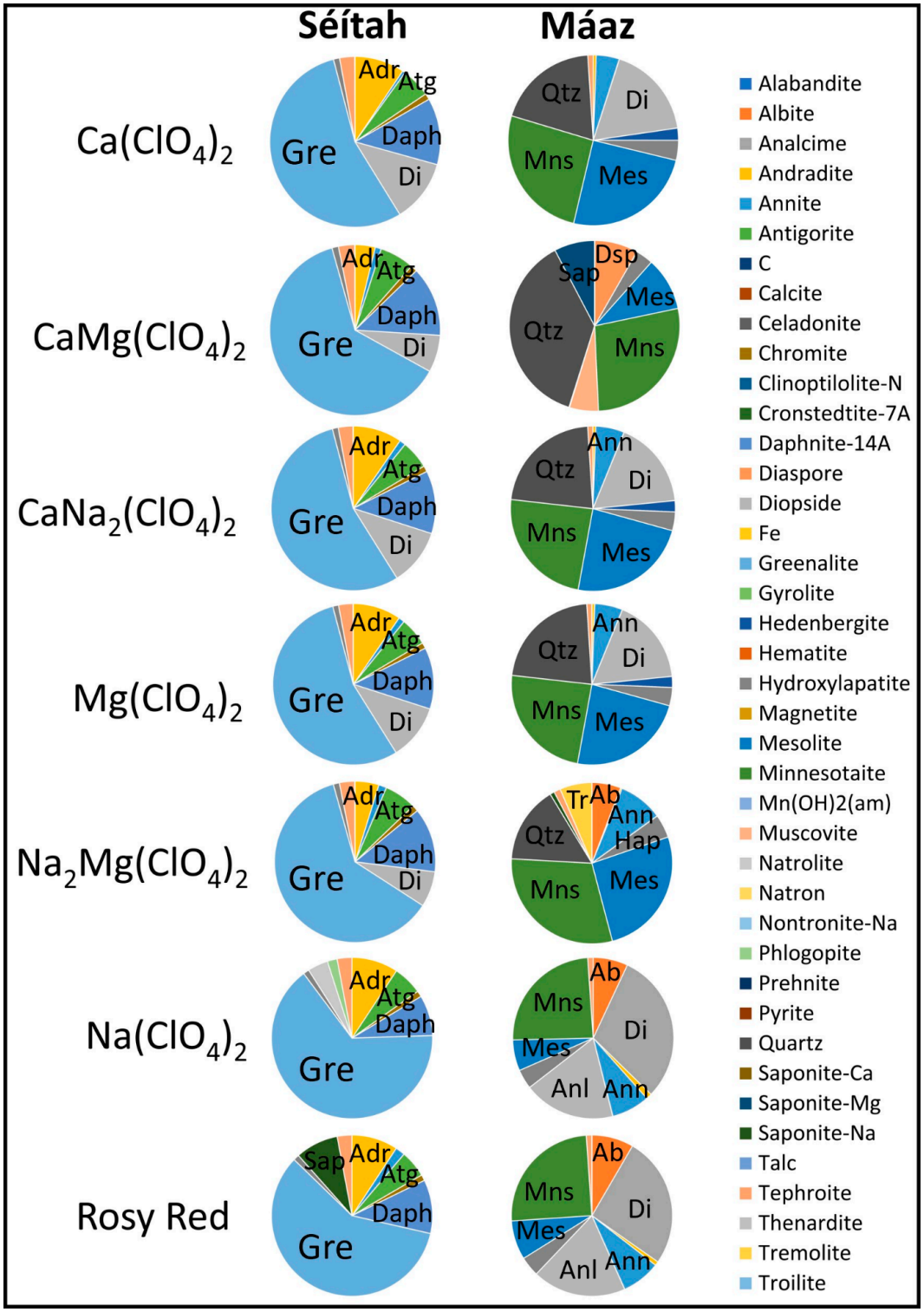

Figure 3. Predicted mineral assemblages at equilibrium as pie charts of molar abundances for the Séítah and Máaz models, with a suite of reasonable planetary waters, at 373.15 K. Major mineral phases are labelled using traditional conventions: Albite (Ab), Analcime (Anl), Annite (Ann), Andradite (Adr), Antigorite (Atg), Celadonite (Cel), Daphnite-14Å (Daph), Diaspore (Dsp), Diopside (Di), Greenalite (Gre), Hydroxyapatite (Hap), Mesolite (Mes), Minnesotaite (Mns), Quartz (Qtz), Saponite-Mg (Sap), Tremolite (Tr). Note that models produced pure C and Fe phases; these may well be amorphous phases rich in those elements, or poorly modeled secondary silicates, oxyhydroxides, or salts.

3.2. Statistical Analysis of Simulation Results

Robust principal component analysis (RPCA) on covariances was completed and spectral decomposition determined the eigenvalues of the equilibrium modeling of the mineral data. The impact of extreme values was effectively damped, as recommended by Zuo (2013). RPCA results show that the first three principal components, PC1, PC2, and PC3, together account for greater than 95% of the variance in the modeled dataset (Figure 4). Eigenvalues based on covariances for the mineral groups are driven largely by PC1 (>64.17% of the variance), driven by positive loadings of "diopside" (~0.991), "tremolite" (~0.676), and, to a lesser extent, greenalite (~0.498) and prehnite (~0.429). The negative loadings in PC1 are the minerals of antigorite (~−0.661), daphnite-14A (~−0.434), "chromite" (~−0.427), and magnetite (~−0.370).

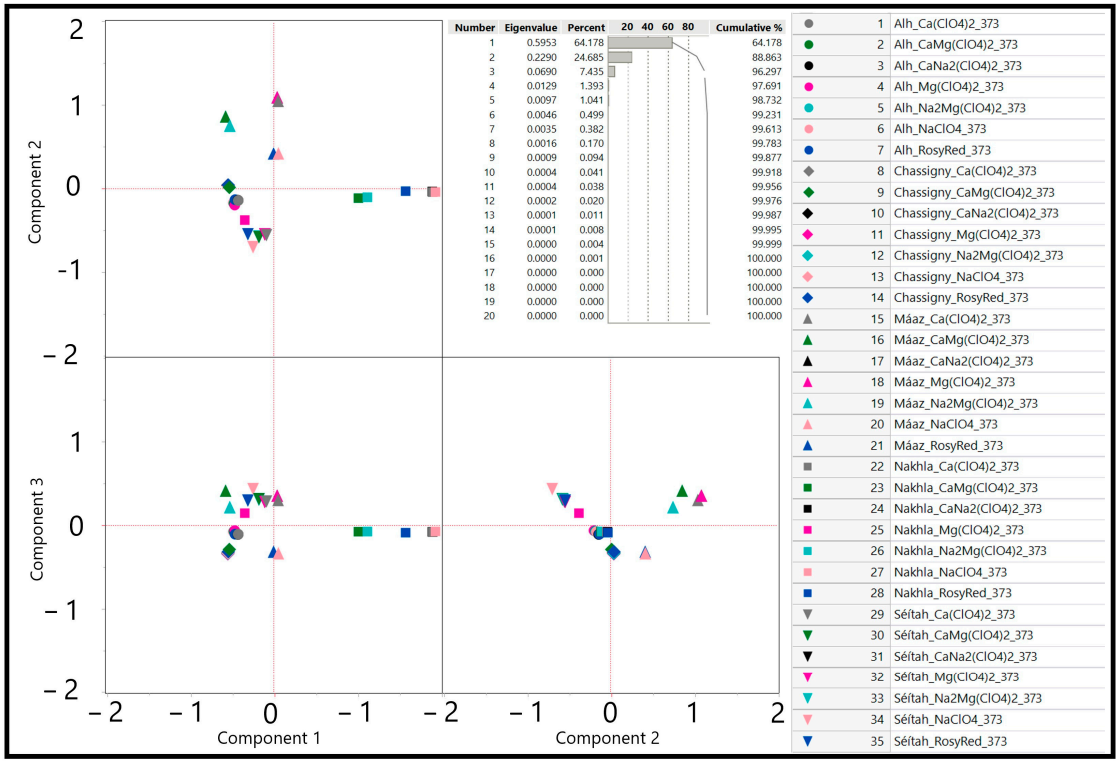

Figure 4. Robust principal component analysis of equilibrium molar abundances of minerals produced. Symbol shape indicates protolith: circles, ALH77005; diamonds, Chassigny; squares, Nakhla; triangle pointing up, Máaz; triangle pointing down, Séítah. Colors of symbols reflect water type. Scree plot shows eigenvalues and percentage of eigenvector influence. See embedded legend. Eigenvalues are based on data covariances.

PC2 (~24.68% of the variance) is largely controlled by the positive loadings from the minerals of mesolite (~0.874), minnesotaite (~0.874), quartz (~0.811), and hydroxylapatite (~0.806). Negative loadings on PC2 were greenalite (~−0.771), daphnite-14A (~−0.649), andradite (~−0.579), and antigorite (~−0.578). PC3 (~7.44% of the variance) is largely controlled by quartz (~0.519) and magnetite (~−0.628).

The score plot conveying the interactions of PC1 and PC2 (Figure 4) shows four clusters in the first, second, third, and fourth quadrants. In the first-quadrant–second-quadrant border, the four simulations are the Máaz protolith simulations with $Ca(ClO_4)_2$, $Mg(ClO_4)_2$, $NaClO_4$, and Rosy Red. The second cluster clearly in the second quadrant includes Máaz protolith simulations with $CaMg(ClO_4)_2$ and $Na_2Mg(ClO_4)_2$. The third cluster in PC1 and PC2 includes the majority of the simulations, all of the Chassigny, ALH77005, and Séítah protoliths, across all water types. The fourth cluster in PC1 and PC2 is composed of the Nakhla protolith simulations. Strong geochemical control of the Máaz and Nakhla

protoliths is supported. Overall, there is greater dispersion in the first and third clusters when compared to the second.

3.3. Bioenergetics

We considered the metabolic reactions for sulfate reduction, methanotrophy, methanogenesis, and anaerobic methane oxidation (AMO), determining each of these metabolic pathways' theoretical bioenergetic energy yield. Modeled activity values were extracted from Geochemist's Workbench REACT modeling output files, and used to calculate the thermodynamic feasibility of these reactions, to connect trace-mineral occurrences to pore-space/fracture-network habitability (see Supplementary Table S4 for relevant bioenergetic-species activities). The reactions modeled were nearly all energetically favorable (Figure 5), apart from two reaction models for methanogenesis, although important geochemical triggers vary across models. These two reaction paths, both Máaz protoliths with $CaMg(ClO_4)_2$ and $Mg(ClO_4)_2$ for methanogenesis, exhibited near-zero Gibbs Free Energy values. Relatively subtle changes in the system geochemistry or environmental parameters could shift methanogenesis into a thermodynamically spontaneous space. In other words, upticks in carbon dioxide and hydrogen concentrations or acidity, or sufficient drawdowns in reaction products, could cause these reactions to be energy-yielding. Conversely, the other metabolic reactions are largely exergonic, with sulfate reduction (~−40 to ~−222 kJ/mol), methanogenesis (apart from the two mentioned above) (~−4 to ~−143 kJ/mol), and AMO (~−37 to ~−78 kJ/mol) all considered favorable, under the modeled conditions.

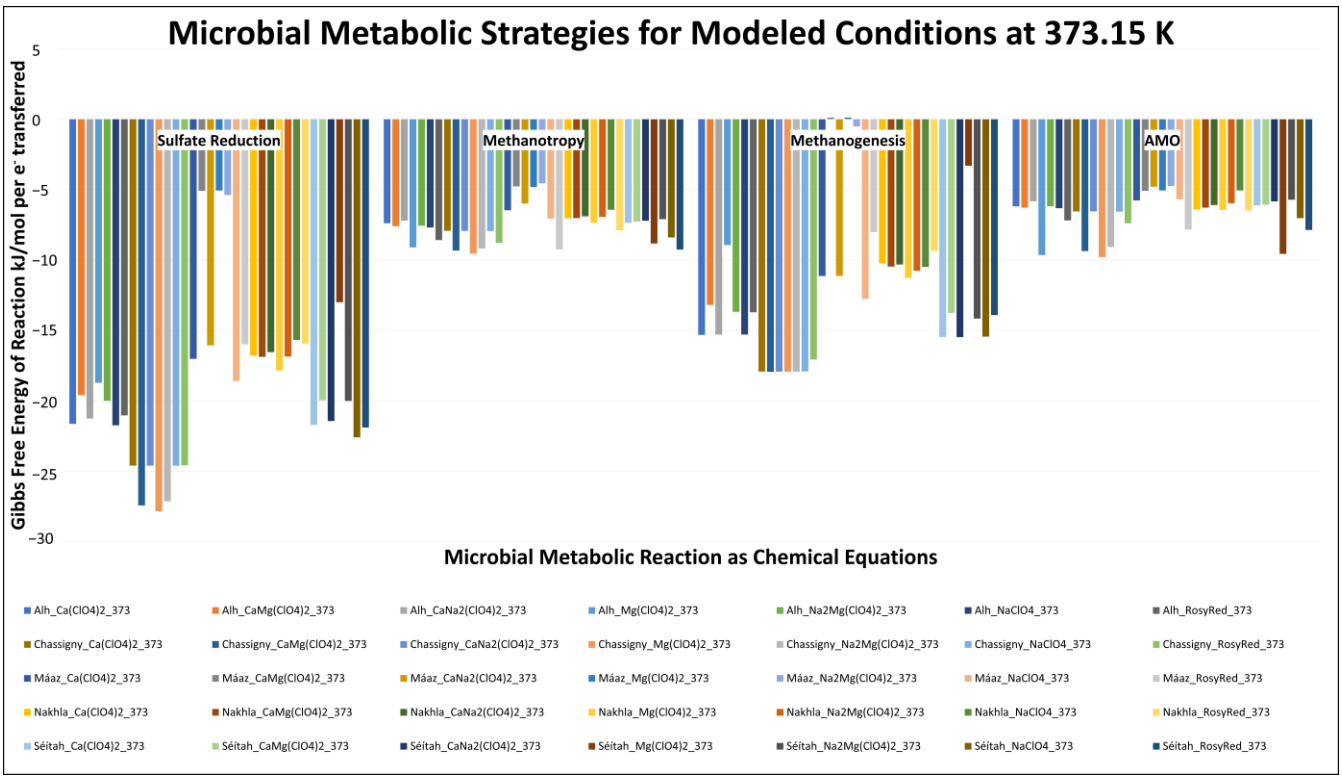

Figure 5. Bioenergetic results from the modeled simulations showing the feasibility of sulfate reduction, methanotrophy, methanogenesis, and anaerobic methane oxidation (AMO), based on Gibbs Energy quantification. All reactions at equilibrium are exergonic at all modeled conditions. Computed Gibbs Free Energy of Reaction is displayed as kJ/mol per e^- transferred in the given reaction.

For sulfate reduction, all meteorite protolith-based reaction path models created promising conditions, and were more favorable for sulfate reduction (Gibbs Free Energy values between ~−125 and ~−222 kJ/mol), than were the Máaz and Séítah models (values between ~−40 and −180 kJ/mol). The greatest bioenergetic yield, herein defined as

the more thermodynamically favorable negative ΔG_r value for the modeled reaction, resulted from the Chassigny model with the $Mg(ClO_4)_2$-type water (~−222 kJ/mol); the lowest yield resulted from the Máaz model with the $Mg(ClO_4)_2$-type water (~−40 kJ/mol). With respect to sulfate reduction, a general bioenergetic ladder can be constructed as a function of protolith type. From most-to-least favorable for most waters, the protolith types accompanying sulfate reduction would be the following: Chassigny > Séítah > ALH 77005 > Máaz > Nakhla. The exception to this general order was the Séítah reaction with $Mg(ClO_4)_2$. Specifically, for the three meteorite protoliths, ΔG_r values for sulfate reduction are sequentially less energy yielding when arranged in terms of protolith type: ~−222 to ~−196 kJ/mol; ~−173 to ~−149 kJ/mol; and ~−142 to −125 kJ/mol. For the Séítah and Máaz models, the calculated Gibbs Free Energy values for Séítah were greater than all of the respective water reactions with Máaz. There were also differences in the rankings of each specific order of favorability of waters reacting with the protoliths, with only Máaz and ALH 77005 being in the same order. For the Séítah and Máaz models, the calculated Gibbs Free Energy values were similar, but less regular: ~−136 to ~−173 kJ/mol for $Ca(ClO_4)_2$; ~−40 to ~−159 kJ/mol for $CaMg(ClO_4)_2$; ~−128 to −171 kJ/mol for $CaNa_2(ClO_4)_2$; ~−40 to ~−103 kJ/mol for $Mg(ClO_4)_2$; ~−43 to −159 kJ/mol for $MgNa_2(ClO_4)_2$; and ~−148 to ~−180 kJ/mol for $NaClO_4$. There was a large range in the values, of ~−127 to ~−175 kJ/mol, for Rosy Red.

In our model, methanotrophy was favored across all reaction paths, with energy values between −77 and −36 kJ/mol. The greatest bioenergetic yield resulted from the Chassigny model with the $Mg(ClO_4)_2$-type water (~−76 kJ/mol); the lowest yield resulted from the Máaz model with the $MgNa_2(ClO_4)_2$-type water (~−36 kJ/mol). The Chassigny models were greater than the other meteorite protoliths for the same water type, with ALH 77005 greater than Nakhla. There was diversity within the protolith reactions, with similarities in most energetically favorable waters, with $Mg(ClO_4)_2$ for Chassigny and ALH 77005. Séítah, Máaz, and Nakhla all exhibited the highest methanotrophic bioenergetic yield with the Rosy Red water. For Nakhla, the range of energy yields was the least among the water types (~−11 kJ/mol), with Chassigny (~−12 kJ/mol), ALH 77005 (~−15 kJ/mol), and Séítah (~−17 kJ/mol) having less range than Máaz-based reactions, which showed the largest range (~−37 kJ/mol). Within methanotrophy only, the Rosy Red waters were the highest-yielding waters for most of the protoliths.

Regarding methanogenesis, the meteorite-based models were generally more energetically favorable (ΔG_r values between −112 kJ/mol and −165 kJ/mol) than the Séítah- and Máaz-based models. Generally, protolith type controlled the feasibility of methanogenesis as calculated here. The greatest energy yield was from the Chassigny model (between −144 and −136 kJ/mol), followed by the Séítah site and ALH 77005, in all reactions except $Mg(ClO_4)_2$, between −124 and −105 kJ/mol. The ALH 77005 and Séítah reactions with $Mg(ClO_4)_2$ were ~−71 kJ/mol and ~−26 kJ/mol, respectively. The Nakhla meteorite models yielded between −90 kJ/mol and −74 kJ/mol. For the Máaz-site models, the reaction path with $NaClO_4$ water was the most energetically favorable, at ~−102 kJ/mol, while the reaction with $CaMg(ClO_4)_2$ water was the least favored. In fact, near-zero but positive (not favorable) ΔG_r values were calculated for the lowest energy yield resulting from the Máaz reaction path with $CaMg(ClO_4)_2$- and $Mg(ClO_4)_2$-type waters (~1 kJ/mol).

Anaerobic methane oxidation (AMO) was thermodynamically favored in all of the models, generally with negative values of tens of kJ/mol; the greatest bioenergetic yield was for the Chassigny model reacting with the $Mg(ClO_4)_2$ water type (~−78 kJ/mol) and the lowest was for the Máaz-site model reacting with $MgNa_2(ClO_4)_2$ water type (~−37 kJ/mol). Models following this were (i) Chassigny, ALH 77005, and Séítah, reacting with $Mg(ClO_4)_2$ water, and (ii) Chassigny reacting with $CaMg(ClO_4)_2$ waters and $MgNa_2(ClO_4)_2$, which had values between −79 and −72 kJ/mol; all others resulted in ΔG_r values between −53 and −37 kJ/mol. Séítah, Máaz, and Chassigny models reacted with Rosy Red water to generate geochemical conditions producing ΔG_r values of between −63 and −59 kJ/mol. Lower ΔG_r values were calculated for Chassigny models with $NaClO_4$, $CaNa_2(ClO_4)_2$, and $Ca(ClO_4)_2$

waters, and also for Nakhla models with Rosy Red, $Mg(ClO_4)_2$, and $Ca(ClO_4)_2$ waters. The least-favorable ΔG_r values were calculated for AMO in the Máaz models, when reacting with $CaMg(ClO_4)_2$, $Mg(ClO_4)_2$, $CaNa_2(ClO_4)_2$, and $MgNa_2(ClO_4)_2$ waters, and also for Nakhla models reacting with $NaClO_4$. These hovered between −41 and −37 kJ/mol.

4. Discussion

Geochemical model results (Figure 2) and subsequent bioenergetics calculations (Figure 5) support multiple fundamentally habitable geologically recent paleoenvironments on Mars, capable of leaving mineral signatures durable enough for long-term detection. To aid comparisons, many primary and secondary minerals detected on Mars in the published literature are provided in Supplementary Table S5; all minerals represented in new model outputs are listed in Supplementary Table S6. As described below in detail, most modeled mineral products are known to occur on Mars, and have been reported previously [157]; the exceptions are andradite, annite, celadonite, and alabandite. Given this reality check, the carbonates, oxides, hydroxides, sulfates, sulfides, and diverse secondary silicates described below are feasible in the Martian shallow subsurface.

4.1. Indicator Minerals of Past Serpentinization (ALH, Chassigny, Nakhla, Séítah)

Serpentine group minerals have been identified on Mars, in layered outcrops, knobby terrain, carbonate plains, the Nili Fossae floor, the wall of the Nili Fossae main floor, impact craters, the Syrtis Major lava flow, heterogeneous terrain, and mélange terrains [47,52]. Recent geochemical and mineral observations at Jezero Crater by the Mars 2020 Perseverance rover show that Séítah formation rock units (with the Dourbes rock sample classed as an ultramafic wehrlite) contain olivine (~65 vol. %), pyroxene (~13 vol. %), and secondary minerals (~12 vol. %) [29]. Further, alteration evidence at these sites includes silicate minerals, Fe-Mg carbonate, and Fe-Mg-Ca sulfate [28]. Given recent discussions of methane on Mars [157–166], and the potential detections of methane from the Nili Fossae in particular [159,160], altered/altering serpentinites and prospective methane fluxes remain of high scientific interest. Mars-wide serpentine distribution data [50,161,162] set the stage for the investigation of higher-resolution phyllosilicate-bounded permeability networks with fracture-zone habitat and (possibly) channelized transfer of methane from depth to the planetary surface.

Modeling and experimental and analog investigations of low-temperature rock alteration applied to Martian environments yield similar results to the mineral assemblages produced here (e.g., [6,64,66,76,86,87,89,129,163–171]). For example, Griffith and Shock [87] modeled the reaction of Icelandic igneous rocks with CO_2-charged water as an analog for Martian meteorite alteration, using the EQ3/6 software package [version 7]; temperatures were elevated compared to the current study, by 50 °C (the lowest temperature modeled was 423.15 K), yet produced similar minerals—antigorite, annite, phlogopite, daphnite, prehnite, tremolite, andradite, calcite, diopside, hedenbergite, magnetite, albite, quartz, and troilite [87]. Bridges et al. [172] reviewed SNC meteorite mineral assemblages and documented clay minerals in Nakhla, and suggest magnesite, calcite, and the gypsum in Chassigny. Berger et al. [173] used EQ3/6 [version 3245, database R54] to react basalt with a $CaCl_2$ brine, and produced similar minerals to this study—Fe, Mg-clay minerals, zeolites, pyroxene, amphibole, epidote and garnet, at 373.15 K. The modeling produced by Berger et al. [173] suggests that the pyroxene and amphibole phases are kinetically inhibited. Catalano [174] performed alteration modeling of Martian basalt at 373.15 K also, using an older version of the Geochemist's Workbench (ver. 9.0.1) and the Lawrence Livermore National Laboratory thermochemical database V8 R6. Their initial conditions were quite different, focusing on Martian basalts reacting with three dilute H_2SO_4 waters ($10^{-2.5}$ to 10^{-1} m) under CO_2 partial pressures of (pCO_2 between 10^{-8} and 10^{-1} bar). Although these simulations were different water–rock reactions, the simulations yielded similar mineralogical products to our results, notably Fe/Mg saponite, serpentine, and zeolites.

Despite inherent limitations in any database, these diverse models, employing different modeling platforms and selecting different input model components, approximate the same results and correspond to Mars surface observations. Common products across the models are antigorite, cronstedtite-7Å, and greenalite (all serpentine-group minerals). Smectite-group clays such as saponite-Ca, -K, -Na, and nontronite-Ca have been identified on Mars [175–177], as have talc [50,64] and chlorite-group minerals [107,175,178–180]. Daphnite-14Å (a chlorite), and a diversity of minor minerals that may not be spectrally resolvable (e.g., fine, dispersed metals, such as sphalerite, see Table 1), are also predicted to occur. Spectrally identified serpentine- and smectite-group clays, along with olivine, at/near the Nili Fossae carbonate plains correspond well with our results (e.g., CRISM observations FRT000028BA_07 and FRT0000A09C_07, [50]). Specifically, Amador et al. [50] describe serpentine- and smectite-group clay detections that correspond with modeled results for (a) Nakhla reactions with $Mg(ClO_4)_2$ and $NaClO_4$ waters, (b) ALH77005 reactions with $NaClO_4$ and Rosy Red, and (c) Séítah reactions with Rosy Red.

Table 1. Indicator minerals of specific water–rock reaction paths, modeled at 373.15 K. Not all reaction paths produced diagnostic mineral groups. Key indicator minerals were saponite-Na, minnesotaite, "tremolite", and zeolite-group minerals.

Protolith	Water	Indicator Minerals Present at Equilibrium
ALH77005	$NaClO_4$	Saponite-Na
	Rosy Red	Saponite-Na
Chassigny	$Ca(ClO_4)_2$	"Fe", Magnetite
	$CaMg(ClO_4)_2$	"Fe", Magnetite
	$CaNa_2(ClO_4)_2$	"Fe", Magnetite
	$Mg(ClO_4)_2$	"Fe", Magnetite
	$MgNa_2(ClO_4)_2$	"Fe", Magnetite
	$NaClO_4$	"Fe", Phlogopite
	Rosy Red	"Fe", Phlogopite
Nakhla	$Ca(ClO_4)_2$	Minnesotaite, Prehnite, "Tremolite"
	$CaMg(ClO_4)_2$	"Tremolite"
	$CaNa_2(ClO_4)_2$	"Tremolite"
	$Mg(ClO_4)_2$	Saponite-Ca, "Tremolite"
	$MgNa_2(ClO_4)_2$	"Tremolite"
	$NaClO_4$	Saponite-Na, "Tremolite"
	Rosy Red	Minnesotaite
Máaz	$Ca(ClO_4)_2$	Minnesotaite, Quartz, Alabandite, "Hedenbergite"
	$CaMg(ClO_4)_2$	Minnesotaite, Quartz, Nontronite-Na, Pyrite, Diaspore, Muscovite, Saponite-Mg
	$CaNa_2(ClO_4)_2$	Minnesotaite, Quartz, Alabandite, "Hedenbergite"
	$Mg(ClO_4)_2$	Minnesotaite, Quartz, Alabandite, "Hedenbergite"
	$MgNa_2(ClO_4)_2$	Albite, Minnesotaite, Quartz, Saponite-Na, Pyrite, "Tremolite"
	$NaClO_4$	Albite, Minnesotaite, Analcime
	Rosy Red	Albite, Minnesotaite, Analcime
Séítah	$NaClO_4$	Natrolite, Phlogopite
	Rosy Red	Saponite-Na

A new interpretation of the presence/absence of minor minerals, arguably diagnostic for the specific rock–water reaction paths modeled here, suggests geologically recent paleowater geochemistry and geologically recent-past microbial metabolic opportunity. All protoliths had at least two scenarios where indicator mineral groups were clear (Table 1).

- For ALH77005 models, trace saponite-Na was produced in $NaClO_4$ and Rosy Red models.

- Chassigny models produced "Fe" and magnetite for $Ca(ClO_4)_2$, $Mg(ClO_4)_2$, $MgNa_2(ClO_4)_2$, $CaNa_2(ClO_4)_2$, and $CaMg(ClO_4)_2$ waters, and produced "Fe" and phlogopite in $NaClO_4$ and Rosy Red solutions.
- Nakhla models yielded "tremolite" in all reactions except the Rosy Red, which uniquely produced only minnesotaite; additionally, saponite-Ca was produced in the $Mg(ClO_4)_2$ model, saponite-Na was produced in the $NaClO_4$ model, and minnesotaite with prehnite accompanied tremolite in the $Ca(ClO_4)_2$ model.
- In Séítah models, the minerals produced in the $NaClO_4$ model were natrolite and phlogopite; the Rosy Red solution uniquely produced saponite-Na.

In general, minor minerals in modeling outputs have been identified/discussed in the Mars-relevant surface mineralogy literature (cf. [179]). In this context, mesolite (zeolite group) has been discussed [133], and populates model results. Tremolite, a common amphibole-family phase in the model results in this work, relates to inferred phases on Mars, such as mixtures of smectites and hornblende [177], and there have been amphibole phases (assumed to be primary) identified in the Tissint Martian meteorite [181]. Al-smectites are reasonable amphibole-weathering products [178]. Additionally, Mars observations of sulfur-bearing phases ranging from gypsum [182] to pyrite [183], and iron-rich phases such as hematite [184–187] and magnetite [188], are consistent with model results.

4.2. Indicator Minerals for Mafic Unit Alteration (Máaz)

Basalt has been identified on the Martian surface via orbital spectroscopic data (e.g., [189–192]) and rovers [27–29,70,125,188,193–204]. The Mars meteorite record includes mafic rocks such as basaltic shergottites, gabbroic shergottites, and many nakhlites (e.g., [21,125,205,206]).

Basalts on Mars range in age and degree of alteration [204], and significant weathering of basalts is implied by many Mars surface observations [207,208]. Mars locations display hematite [209], gypsum [210–213] carbonate and perchlorates [36,132], and sulfates and silica [204]. Additional secondary minerals such as prehnite, illite/muscovite, serpentine, opaline silica, and the zeolite mineral analcime [175,177,179,214] have been reported. Clay minerals like nontronite [45,215], Mg-smectites [175], aluminum phyllosilicates, kaolinite, beidellite, and montmorillonite are known to occur, with and without nearby hydrated silica [45,216,217]. The Máaz reaction-path models showcase mafic rock alteration as a function of water type, and provide grounds for comparison with existing data for Mars surface mineralogy.

In Máaz models, for all paths, minnesotaite was produced. Quartz was produced in $Ca(ClO_4)_2$, $Mg(ClO_4)_2$, $CaNa_2(ClO_4)_2$, $CaMg(ClO_4)_2$, and $MgNa_2(ClO_4)_2$. Co-occurring minerals differed. $Ca(ClO_4)_2$, $CaNa_2(ClO_4)_2$, and $Mg(ClO_4)_2$ water types all produced minnesotaite and quartz with alabandite and hedenbergite. Both the $NaClO_4$ and Rosy Red water types produced minnesotaite with albite and analcime. Both $CaMg(ClO_4)_2$ and $MgNa_2(ClO_4)_2$ water types reacted to give unique indicator-mineral results. In the $CaMg(ClO_4)_2$ reaction, indicator minerals include nontronite-Na, pyrite, diaspore, muscovite, and saponite-Mg, added to the quartz and minnesotaite background. In the $MgNa_2(ClO_4)_2$ reaction, albite, saponite-Na, pyrite, and tremolite were present, added to the quartz and minnesotaite background.

The minerals so produced are known in the terrestrial basalt record, and validate the modeling approach. Terrestrial basalts which are altered in marine environments, typically exhibit selective mineral solution and replacement with secondary minerals, over time. Classic processes active in basalt alteration under diagenetic conditions (arguably through the onset of low-grade metamorphism) include albitization or spilitization, zeolitization, and rodingite formation (or rodingitization) (e.g., [218]).

Albitization/spilitization generally encompasses the transformation of Ca-rich plagioclase to albite at low temperatures, when Na^+-bearing waters flow through basalts over time. Recall that higher-temperature albitization has been observed for decades in natural environmental samples and experimental data [219], and hydrothermal alter-

ation of terrestrial basalts has conventionally been assigned a mineralogical assemblage of albite-actinolite-chlorite epidote, with quartz and pyrite as possible accessory phases [220]. The modeled increases in albite, chlorite, and quartz certainly correspond to well-known terrestrial basalt alteration.

Zeolites are hydrous aluminosilicates that have great capacity for ion exchange. Zeolitization has typically been associated with mafic glass alteration or cavity-filling mineralization in vesicular basalt. In fact, seabed coring e.g., [221] has often documented pervasive zeolite formation, with calcite mineralization as a late-stage process. In other locations, mineral zonation observed within the zeolite-group minerals has allowed generations of low-temperature alteration to be resolved. In thickly stacked basalt flows of Iceland and East Greenland, experiencing burial metamorphism in the presence of advecting waters, analcime was detected in subsurface horizons ~600 to 750 m and 500 to 800 m below the top of the basalt pile, with mesolite detected at adjacent, deeper intervals [222]. Zeolite zonation, given distinct temperature gradients, has been highlighted in Icelandic geothermal systems: mesolite has been associated with 343.15 K to 363.15 K alteration temperatures, and analcime with the 503.15 K to 573.15 K interval [222]. Alterations in volcaniclastic sediments in Japan resulted in clinoptilolite and analcime forming in temperature ranges of 333.15 K to 357.15 K and 364.15 K to 393.15 K, respectively [222]. In West Greenland basalts, regionally low geothermal gradients (<45 °C/km) drive the formation of sequential classes of zeolites, with some incorporation of 'mafic phyllosilicate' material [223]. Weisenberger and Selbekk [224] documented analcime and mesolite in Iceland's Hvalfjordur basalt flows, post low-temperature alteration, with robust phase detections. Fresher water systems (continental environments) also likely host zeolite formation, as shown experimentally [225], and increasingly in field observations [222].

The case of rodingitization is particular, and geochemically very specific: calcium-rich waters acting on mafic lithologies (Ca-metasomatism), often associated with serpentinization [226], drive the formation of specific low pressure–temperature mineral assemblages including prehnite, tremolite, diopside, hydrogarnet, epidote or clinozoisite, chlorite, calcite, and rare titanite, apatite, and zircon [226–231]. Many of these minerals occur in model outputs. The common terrestrial rodingite-mineral features, functionally controlled by the availability of Ca^{2+}-bearing terrestrial waters, might necessarily be replaced by Na^{+} or Mg^{+} mineral phases, based on the major cation inventories in the modeled waters.

4.3. Bioenergetic Implications

Subsurface serpentinization provides the necessary chemical energy to support microbial metabolisms, both on Earth and beyond ([1,149,232–237]; this work). The challenge of approximating extraterrestrial growth conditions has been innovatively approached. Using a Chassigny-type protolith, Ref. [238] showed that it is possible to produce approximately 26 g of biomass using chemical energy derived from water–rock reactions. Here, water–rock mass ratios were defined as nearly 1:1, relatively low ratios, indicating slow or low-volume percolation of reactive water in the system. There are further factors needed to make a particular environment important for astrobiology, such as conducive geophysical conditions like planetary mass and size, stable temperature, protection from galactic cosmic radiation, etc., and star–planet interactions.

When computed based on activity data in modeling outputs (see Figure 5), we show that the spontaneous reactions are the following: sulfate reduction coupled with H_2 oxidation; methanogenesis, using CO_2 as the carbon source to be reduced, coupled with H_2 oxidation; and anaerobic methane oxidation (to aqueous CO_2), coupled with sulfate reduction.

Aqueous alteration of mafic rocks certainly influences the subsurface bioenergetics in terrestrial mafic-rock units, though chemically and energetically distinct from serpentinization processes. Hot, young mafic crusts, with abundant ferrous iron, can facilitate diverse Fe oxidation reactions, but cooler microbial ecosystems may shift to take metabolic advantage of radiolytic hydrogen production as the key electron donor [239]. When olivine-rich lithologies experience low rates of water flow through the permeable matrix, hydrogen is

not lost as rapidly, and may host significant hydrogenotrophic activity [240]. The cooler systems are the more apt comparisons here.

The bioenergetic implications of our modeling are that there are high-, moderate-, and low-yield metabolisms, feasible across the water types considered. High-yield metabolisms involve sulfate reduction and methanogenesis (~−100 to −250 kJ/mol). Moderate-yield (between −100 and −50 kJ/mol) and low-yield (>−50 kJ/mol) metabolisms involve a few methanogenesis reactions, along with all methanotrophy and anaerobic methane oxidation (AMO) reactions.

When methane oxidation (to aqueous CO_2) is coupled with sulfate reduction (to $H_2S_{(aq)}$), the ΔGr of methanotrophy is strongly positive (non-spontaneous) in every modeled case, at every condition. Very little variation exists in the overall energetics of the reaction, based on the modeled conditions. Our results are within the range of results obtained by Marlow et al. [235], who investigated seven fluids and calculated methane oxidation using the same summarized metabolic reaction, obtaining values between −31 and −135 kJ/mol. Differences in our calculations likely reflect differences in model structure and the decision to allow planetary fluids or Martian groundwaters to react only with the Martian atmosphere [235], rather than investigating the subsurface water–rock system (this study).

Note that bioenergetic calculations for reactions discussed here give numerical results that are an order of magnitude less than those reported in Oze and Sharma [20]; we present ΔG_r (tuned to activity data in model results), while standard-state (ΔG_r°) values were discussed conceptually in the work of Oze and Sharma [20]. Model outputs in this study are thermodynamically stable at equilibrium, and mineral assemblages are consistent with other work on the low-temperature alteration of mafic- and ultramafic-phase equilibrium models on Mars [241]. Kinetic considerations are important to real-weathering and low-temperature alteration processes at/near the surface of Mars, but are beyond the scope of this work. Within the paragenesis of water–rock settings with astrobiological implications, such as these, it is important to recognize that, although the temperature is relatively low for geological processes, alteration of primary minerals to secondary phases is possible, for example by protons or catalysts that weaken surface charges and atomic bonds [173]. Further, this process is still being explored kinetically, and an example of this is the transition of smectite to illite, shown in similar quasi-diagenetic alteration conditions [242–244]. In addition, some high-temperature minerals, such as fayalite, have been suggested to form far below convention, at 573 K, in a Washington State gold mine [245]. The thermodynamic stability and challenges to conventional kinetic limitations have also been explored in space materials, including carbonaceous chondrite MAC 88107, suggesting that 423 K to 473 K aqueous alteration can produce iron-rich olivine, via precipitation [246].

4.4. Precedents from Similar Terrestrial Microbial Ecosystems

As Baas Becking stated in 1934—the environment selects for the life it hosts. Chemolithoautotrophic organisms are driven by chemical energy obtained from the Earth's lithosphere everywhere beyond the reach of sunlight, where temperature and other conditions allow. In continent-hosted serpentinite aquifers, similar water–rock reactions impact subsurface groundwater ecosystems [151,152,247–253] (Supplementary Table S1). In the Coast Range Ophiolite, USA (e.g., [254,255]), the Samail ophiolite in Oman (e.g., [256–258]), the Bay of Islands Ophiolite in Newfoundland, Canada (e.g., [259,260]), the Santa Elena Ophiolite, Costa Rica (e.g., [261]) and others, serpentinization influences biogeochemical cycles tuned to the geochemistry of the environment. Extraterrestrial environments could host similar biotic processes [7,50,54–56,71,161,260].

Possible sites of serpentinization-driven metabolic systems have also been identified, such as the Alter-do-Chão massif [262] and the Ronda massif [263]. Notably, at the Outokumpu deep drill hole, serpentinization at depths between 1.3 and 1.5 km drives carbon assimilation, methanogenesis, nitrate reduction, and sulfate reduction [264]. This particular site is analogous to sites in the Martian crust and upper lithosphere, where the

habitable volume encompasses depths of 6–8 km, before reaching upper temperature limits for life [39].

The subsurface seabed (sedimentary blanket and mafic-to-ultramafic rocks of the oceanic lithosphere) supports an array of metabolisms. Where serpentinization occurs in fault-translated or underlying ultramafic units, it generates redox gradients and a long-lived source of carbon (organic acids and methane, reworked from ocean-derived inorganic and organic compounds) and of electrons (generally, but not exclusively, via H_2 oxidation). Deep sediments support sulfate reduction (e.g., sulfate-reducing methanotrophy, [265,266]), as do vigorous, widespread hydrothermal vent systems [267–271] and paleo-hydrothermal environments, such as Río Tinto in the Iberian pyrite belt [272]. Methane cycling has been closely studied in marine vent systems, such as at the low-temperature Lost City Hydrothermal Field [273,274], and higher-temperature vent systems, like the Rainbow and Logatchev Mid-Atlantic Ridge sites [271]. In more recent studies of microbial colonization of ultramafic materials in a seabed-simulation experiment, special emphasis has been placed on prospects for H_2 scavenging and its efficient utilization in the seabed [275].

Water–rock interactions fuel the deep biosphere in the terrestrial mafic–ultramafic subsurface, at temperatures most often above 274.65 K to ~310.15 K (e.g., the ophiolite-hosted groundwater systems in Gruppo di Voltri, Liguria, Italy, and Oman; see Schrenk et al. [271]), or in seabed vent systems from 313.15 K up to ~653.15 K [271]. A landmark study, although controversial, of the role microbes play in the cool Columbia River Basalt-hosted aquifer revealed a slow but active influence on dissolved H_2 abundances (e.g., [276]).

Life exists in ice, icy-regolith and icy-aqueous settings (oceanic, lacustrine, or pore spaces in sediments), and cold arid deserts [75], and is under close study in permafrost generally [277], with special attention paid to Alaskan permafrost [278]. Further, in cold arctic-lake sediments, terrestrial methanogens such as Methylobacter and Methylomonas show evidence of methane oxidation at extremely low temperatures, down to at least 277.15 K [279]: life persists near the lower-temperature cut-off for survival. Although beyond the scope of this modeled work, the temperature resilience of methanogens and other cryophilic microbes makes them excellent model systems for comparative study, as lower-temperature systems come under scrutiny.

Biogeochemical limits of course constrain life on Earth. In most land-based Earth environments, the rock-hosted shallow biosphere is richly supported by photosynthetic biogeochemical cycles, directly or indirectly, through the decomposition of organic matter produced in sunlit systems (see [75] and references therein, [280–285]). Diverse metabolic pathways and complex ecological relationships exist, and understanding the dynamics of subsurface ecosystems is crucial to applying Earth analog datasets elsewhere. Of special interest are microbes that assimilate carbon as $CO_{2(g)}$ or metabolize other relevant Martian atmospheric gases, such as H_2, CO [286], and CH_4 [287,288].

Microbes carrying out the metabolic reactions tested here include the anaerobic methanotrophic archaea (ANME), for which the mcrA gene was identified at Lost City [289], and methanotrophic bacteria like Methylococcales, also detected at Lost City [271] and at Rainbow [290]. Furthermore, Methanobacterium has been identified at the Zambales [291] and the Del Puerto Ophiolite [292]. Given that methane production is known to occur in serpentinization systems, direct observations of gene sequences associated with methanogenesis have been successful in the Del Puerto Ophiolite [292], the Bay of Islands Ophiolite [250], and at Lost City [273]. Methanogenic archaea have also been observed at the South Chamorro Seamount [292], and archaea in the order Methanococcales were documented at sites in the Mid-Atlantic Ridge, such as at Logatchev and Rainbow. In our bioenergetic models, H^+, SO_4^{2-}, HCO_3^-, S^{2-}, and $CO_{2(aq)}$ were usually the limiting reagents.

In the context of work by Marlow et al. [235], patterns are similar, though Marlow et al. used contrasting fluids and calculated methane oxidation using the same methanotrophy; they summarized the metabolic reaction, and obtained values between −31 and −135 kJ/mol CH_4. However, a key difference between reports is that Marlow and col-

leagues allowed Martian groundwaters to react with the Martian atmosphere; we keep the water–rock reaction path closed in the rock subsurface.

Comparative terrestrial analog studies remain in high demand; terrestrial microbes toggle between different metabolic pathways based on environmental triggers, and there are many plausible dynamic scenarios for different Martian environments. In any case, the absolute habitable volume in the near-subsurface of Mars must vary over space and time. Debate continues about the nature of a shallow-water reservoir on Mars. There may have been 'sporadic' groundwater upwellings on local scales [39], near global groundwater systems [41], and modern groundwater at a depth of several km has been posited [293]. Geomorphology supported by landscape models suggests that numerous short-lived Noachian lake basins were exposed at the planetary surface [294]. In a troubling counterpoint, no shallow Martian aquifer was actually detected in InSight seismometer datasets [295], but there is consideration of possible liquid-phase water via observations of reoccurring slope lineae [296,297].

An important area of future work will be in evaluating the bioenergetics and biomarkers of acetate-producing microbes such as those recently detected in Oman [298] and which are strongly suspected at The Cedars ultramafic-hosted springs in northern CA [299] and the Hakuba Happo hot springs, with some serpentinization-derived mixing component, in Japan [300]. Given the repeated observations of acetate and other organic acids in waters influenced by serpentinization, the growth limits and preferred aqueous environments of known acetate-generating microbes may have profound importance in extraterrestrial settings.

4.5. Modeled Results in the Context of Planetary Science Missions

Recent ground-penetrating radar measurements collected by the Perseverance rover show both fast and slow travel times, indicating that the near-subsurface is heterogeneous [27]. The non-uniform nature of the near-subsurface adds new relevance to this study. Recall that, for the model platform used here (Geochemist's Workbench), the system pressure is set for the system at 1.013 bar: this pressure corresponds to shallow, near-subsurface depths (~9 m). Although some minerals/polymorphs were not present in the thermodynamic database utilized in the modeling (e.g., compositionally diverse brucite minerals), we have described sets of minerals that connect to clearly defined water–rock interaction histories. In other words, the mineral groupings presented here constitute a hydrogeochemical facies model that can be consulted, given mineral observations from Mars and other planetary surfaces with mafic–ultramafic exposures.

With the anticipated future retrieval of rocks cored by the Perseverance rover at the Maaz site, core splits should be screened carefully for indicator minerals such as pyrite, alabandite, and zeolites. Regarding pyrite: modeling the Máaz protolith reactions with $CaMg(ClO_4)_2$ and $Na_2Mg(ClO_4)_2$ generated pyrite. Recall that pyrite has been detected in Martian meteorites ALH 84001 [301] and NWA 7533 [302], and previously on the Martian surface at the Gale crater, in association with clay minerals [183,303]. Regarding alabandite, a rare Mn-sulfide: selected Máaz protolith reactions of $Ca(ClO_4)_2$ and $CaNa(ClO_4)_2$, and the simulations with $Mg(ClO_4)_2$ produced alabandite chemically analogous to pyrrhotite, with diverse cations bonded to sulfur. Regarding zeolites: analcime was produced in the modeling for the models, $Na(ClO_4)_2$, and reactions with Rosy Red co-occurring with smectites, serpentines, magnetite, clinopyroxenes, hematite, and carbonates. Perseverance cores sampled at the Séítah site should be screened for minerals that emerge from ultramafic protolith models, and are diagnostic for specific water types.

For context, Pascuzzo et al. [304] suggest that the Nili Fossae likely had shallow subsurface water–rock reactions and hydrothermal activity. Both Amador et al. [50] and Viviano et al. [64] describe rock alteration scenarios involving serpentinization followed by carbonation of the olivine-rich unit. Serpentinization likely altered the olivine-rich, uppermost unit at the nearby Nili Fossae [46,50,60,61,79,215], specifically in the olivine-rich caprock, between 35 m and 160 m thick [165]. The prospect of a wedge of habitable, evolving ultramafic/mafic material, providing bioenergetic support for life based on these

transparent modeling results, is compelling. In fact, related work on the Nili Fossae suggests fluid-limited carbonation of serpentine at low-temperature ($\leq$200 °C) [64,305,306], immediately relevant to the low-temperature conditions considered in this study.

Another exciting connection with timely investigations related to the Mars 2020 mission rests in the recent detections of organic carbon at specific sites. Recent work by Scheller et al. [307], which analyzed Máaz- and Séítah-formation rocks, identified organic material associated with Na-rich perchlorates in rock units similar to initial and equilibrium assemblages in this study. Interestingly, Scheller et al. [307] noted that serpentine minerals have not been identified yet in the Séítah-formation rocks, yet these remain ultramafic in a geochemical sense; a serpentine phase or a post-serpentine weathering phase (complexly interlayered chlorite–smectite assemblages) would be consistent with our understanding of mineral evolution in these systems.

As an aside, detections of organic molecules in diverse Mars materials are mounting: the Mars meteorite ALH 84001 exhibits organic molecules associated with serpentinization [308], building on much previous work [205,309–315]. Even more profound is the organic-molecule detection in the approximately 3.5 Ga mudstones at Pahrump Hills, Gale crater, by the Curiosity rover [316], and in the atmosphere [147].

Mars hosts diverse minerals related to mafic–ultramafic rocks and their alteration, which have been observed either through rover tools or through remote sensing, and to which the scientific community will shortly have access. At least 160 distinct mineral species have been identified on, or are postulated to be on, Mars [155], Detailed micro- and nano-scale mineralogical study of returned Mars samples after the Mars 2020 mission, ongoing investigations of the Jezero Crater, or future high-res sampling in/around the Nili Fossae region will benefit from targeted modeling results. Key indicator minerals are established for reference in future Mars mission-data reduction, to confirm geologically recent habitability in sampled rocks and related environments on Mars, and to direct follow-on analytical work focused on biomarker detection.

4.6. Modeled Results in the Context of Geologically Recent Habitable Niches

Terrestrial-planet volcanism and impact events drive hydrothermal activity, and the subsequent water–rock interactions have the potential to drive microbial ecosystems (e.g., [1–7,96]). Magmatic and impact-induced hydrothermal activity was periodic throughout the geological history of Mars (e.g., [316] and references therein). Volcanism and impact events can create spatially limited but important geophysical conditions that are sufficient for driving water–rock reactions in microenvironments pertinent to this study.

Scattered throughout the Tharsis region of Mars, evidence of volcanic activity younger than 100 Ma is found the southeast approach to Olympus Mons, the northeast approach to the Ceraunius Fossae, the southeastern approaches to Ascraeus Mons and Pavonis Mons, and the northeast approach to Arsia Mons [317]. New evidence suggests that the Tharsis region on Mars, specifically Alba Mons, has been active continuously, as recently as ~10 Ma, with a large number of ~100 Ma-aged eruptions suspected between 20 and 25° N and 125 and 105° W associated with Alba Mons and the Ceraunius Fossae region [318]. Krishnan and Kumar [318] suggest that the recent tectonic and volcanic activity drove the boulder falls hypothesized to be the epicenter of the observed M_W 4.1 marsquake on 18 September 2021. Serpentine and associated minerals in the Tharsis Montes have been strongly inferred spectrally, but require further characterization [319].

Impact events are geologically pervasive, and can generate significant heat, which will result in the planetary lithosphere having an increase in temperature [320]. Small-impact cratering events, between 5 and 10 km, have the potential to drive hydrothermal systems on Mars [96]. A moderate 30 km-diameter crater on Mars has the potential to fuel a hydrothermal system in the subsurface for ~67,000 years [321]. Further, analysis of analog impact-induced hydrothermal systems found on Earth, such as the relatively small ~4 km-diameter crater at Kärdla, Estonia took between ~1500 and 4000 years to cool to below our model temperature of 373.15 K [322]. Larger, less-common impact events

studied on Earth, such as the ~250 km-diameter Sudbury impact event is likely to have sustained hydrothermal activity for approximately 1 million years [323]. Modeling work associated with the Chicxulub impact, a 180-km-diameter event, suggests 1.5 to 2.3 million years [324].

Impact-induced plausible hydrothermal systems have been charted in diverse terrains on Mars. For context, ancient examples include the Noachian ~153 km-diameter Holden impact crater in the Margaritia Sinus quadrangle [325] and the ~40 km-diameter Hesperian Toro complex impact crater in the Sytris Major quadrangle [326]. Within the geologically recent Amazonian, two craters have been identified that have likely hosted hydrothermal systems; spectral detections of phyllosilicates support this [327] at an unnamed ~20 km-diameter crater in the Ismenius Lacus quadrangle (from [328]: Crater ID 05-000375), and at the ~62 km-diameter Stokes impact crater in the Cerbrenia quadrangle (from [328]: Crater ID 07-0000008). The Ismenius Lacus crater shows spectral evidence of chlorite and Fe-serpentine, where the Stokes impact crater shows spectral evidence of a suite of Fe/Mg/Al phyllosilicates [327].

Given these two impact craters with spectrally defined hydrothermal phyllosilicates, along with appropriate impact-event causes (e.g., no hydrothermalism suspected prior to impact), Turner et al. [327] identified 144 craters $\geq$ 7 km in diameter within the Amazonian. Turner et al. [327] further examined craters with diameters of 3 to 7 km, and found that these craters lacked hydrated minerals in the CRISM data. Further, Turner et al. [327] described hydrothermal systems during the Amazonian period on Mars as sparse processes, not easily detectable at the spectral spatial scale of ~20 to 40 m/pixel resolution of the satellite observations by CRISM. Others have hypothesized that the physicochemical conditions for water–rock reactions associated with impact events could drive habitable environments for extended periods of time [321,329,330]. During the Amazonian, impact-event frequency has been much lower than during the Noachian or Hesperian, but [331,332] indicate that crater diameters between 8 and 64 km, relevant to this study, would occur on the surface of Mars every ~1 million years (in the 8 km-diameter case) or ~100 million years (in the 64 km-diameter case). Smaller craters, such as those with ~1 to 2 km diameters, could occur as frequently as every ~10,000 years (~1 km-diameter case) to ~100,000 years (~2 km-diameter case), but such craters have yet to be identified with hydrothermal mineral assemblages on Mars [327].

Radionuclides have also been considered as a heat source to plausibly spur hydrothermal systems [2,4,331] and subsurface microbial metabolisms in the modern Martian surface (e.g., [76]). Radionuclides, such as U, Th, and K (half-lives in the order of ~ billions of years) have the capacity to drive hydrothermal systems for timescales significantly greater than volcanism and impact events, in the order of >100 million years [331]. Examination of the Martian near-subsurface for areas of high concentrations of Th and K by Ojha et al. [331], showcased the Eridania quadrangle region and Isidis Planitia just southeast of the Nili Fossae, in the Syrtis Major quadrangle. Both sites exhibit spectral evidence of serpentinization via the identification of Fe- and Mg-serpentine and other products [50,332]. Relevant investigation continues also at an analog site on Earth for radiogenic heat-derived hydrothermal systems at the Mt. Gee-Mt. Painter system in the Northern Flinders region of South Australia (MGPS) [331].

Magmatic activity, impacts, and radiogenic heat production are considered the three planetary-scale processes that generate the heat necessary for the water–rock modeling in this study. Temperatures at/near 373 K occur at diagenetic/very low-grade metamorphic conditions [12,13,64,305], and are certainly habitable for life as we know it [39]. Although outside the scope of this study, modeling lower temperatures, between 273.15 K and the temperature limit used in this work, would provide further insight into the thermodynamic stability of phases which may or may not be kinetically limited in the Martian subsurface environment. We look forward to further interrogation of plausible hydrothermal sites and serpentinization in planetary environments, leveraging the fine-tuning (particularly in

terms of solid-phase and aqueous-system geochemistry) possible with a thermodynamic modeling approach.

5. Conclusions

The surface and near-surface of contemporary Mars is frozen, oxidized, and irradiated. However, in the past, Mars likely had habitable conditions with the potential to sustain life [333–338], and may still today hold habitable niches in the subsurface, supported by water–rock reactions. Between 3.5 and 3 billion years ago in Martian history, encompassing the middle-to-late Noachian Era and the early Hesperian Era [334,335], there is evidence that the planet was geologically much more active, and had liquid water (e.g., [134,296,334–336]), but evidence of modern groundwater flows (e.g., [339–344]) excites prospects into a rock-hosted habitable environment within the subsurface of Mars (this work, [76]). Our work shows that the chemical energy available through aqueous alteration of specific units in the Martian lithosphere corresponds to enhanced potential for microbial metabolism, charting a possible pathway for habitability under near-surface geophysical water–rock conditions, at plausible temperatures for proximal geothermal or impact-derived heat. We show that reactions that mirror the known terrestrial microbial metabolisms of sulfate reduction, methanogenesis, methanotrophy, and AMO are spontaneous, from a thermodynamic perspective, and are feasible metabolic strategies for the modeled environment.

A key takeaway of this work is that our models confirm that mineral detections on Mars by the Compact Reconnaissance Imaging Spectrometer for Mars (CRISM) in the Nili Fossae region [46,50] can be produced through past water/rock interactions under geologically recent Martian conditions, with specific water types implicated by minor mineral occurrences. The rocks under study inform ongoing investigations by the Perseverance rover. The water types used to structure the modeled interactions are literature-based, and feature different cation–perchlorate compositions. The overlap between modeled mineral products and the growing lists of minerals detected on Mars is now better contextualized.

Beyond the current Mars mission, other locations on Mars where there is likely serpentine and other minerals predicted in this study include the Claritas Rise, Valles Marineris, North Argyre Basin, Tyrhenna Terra, South Isidis, Nili Fossae, and Terra Sirenum [46,49,50,337–345].

Table 1 provides a condensed summary of indicator minerals that derive from specific water/rock interactions under Martian conditions, and can be used as a reference for screening well-resolved mineralogical data for these 'fingerprints' of geologically recent paleo water activity. Applying these results to the analysis of Mars samples (in situ and when returned to formal laboratory settings on Earth) in future NASA missions is exciting.

Future directions include the incorporation of other Martian crustal compositions with explicit influx of radiolytic hydrogen, and consideration of other possible water types. Better representation of the Martian near-surface environment, and systematic assessment of mineral suppression choices with metabolic considerations, would deepen the model result (cf. [4] on icy satellites). Continued monitoring of terrestrial analog geomicrobiology of continental and submarine serpentinites, basaltic aquifers, and the dynamics and resilience of metabolic pathways used by these organisms on Earth would also help constrain how far we can take modeling in assessing the astrobiological potential of the Martian near-subsurface and similar environments elsewhere. The importance of serpentinization as a spur for life and a sustainer of astrobiology may be far greater than previously assumed.

Supplementary Materials: The following are available online at https://www.mdpi.com/article/10.3390/life13122349/s1, Table S1: Serpentinization Sites, Table S2: Protoliths, Table S3: Aqueous Species, Table S4: Aqueous Species Activities, Table S5: Mineral Products, Table S6: All minerals represented in new model outputs, Figure S1: Model pH.

Author Contributions: Conceptualization, R.H. and D.C.; Methodology, R.H. and D.C.; Software, R.H. and D.C.; Validation, R.H. and D.C.; Formal analysis, R.H. and D.C.; Investigation, R.H. and D.C.; Resources, R.H. and D.C.; Data curation, R.H. and D.C.; Writing—original draft, R.H. and D.C.; Writing—review & editing, R.H. and D.C.; Visualization, R.H. and D.C.; Supervision, R.H. and D.C.; Project administration, R.H. and D.C.; Funding acquisition, R.H. and D.C. All authors have read and agreed to the published version of the manuscript.

Funding: This research was funded by NASA EPSCoR CAN, Award No. 80NSSC22M0177 and National Science Foundation under Award No. 2124859. Any opinions, findings, and conclusions or recommendations expressed in this material are those of the authors and do not necessarily reflect the views of NASA or the National Science Foundation.

Institutional Review Board Statement: Not applicable.

Informed Consent Statement: Not applicable.

Data Availability Statement: All data are available in Supplementary Files.

Acknowledgments: The authors would like to thank the NASA Rhode Island Space Grant community for invigorating research discussions.

Conflicts of Interest: The authors declare no conflict of interest.

References

1. Vance, S.D.; Harnmeijer, J.; Kimura, J.; Hussmann, H.; de Martin, B.; Brown, J.M. Hydrothermal Systems in Small Ocean Planets. *Astrobiology* **2007**, *7*, 987–1005. [CrossRef]
2. Farkas-Takács, A.; Kiss, C.; Góbi, S.; Kereszturi, Á. Serpentinization in the thermal evolution of icy Kuiper belt objects in the early Solar system. *Planet. Sci. J.* **2022**, *3*, 54. [CrossRef]
3. Neveu, M.; Desch, S.J. Geochemistry, thermal evolution, and cryovolcanism on Ceres with a muddy ice mantle. *Geophys. Res. Lett.* **2015**, *42*, 10197–10206. [CrossRef]
4. Neveu, M.; Desch, S.J.; Castillo-Rogez, J.C. Aqueous geochemistry in icy world interiors: Equilibrium fluid, rock, and gas compositions, and fate of antifreezes and radionuclides. *Geochim. Cosmochim. Acta* **2017**, *212*, 324–371. [CrossRef]
5. Glein, C.R.; Baross, J.A.; Waite, J.H. The pH of Enceladus' ocean. *Geochim. Cosmochim. Acta* **2015**, *162*, 202–219. [CrossRef]
6. Daswani, M.M.; Vance, S.D.; Mayne, M.J.; Glein, C.R. A Metamorphic Origin for Europa's Ocean. *Geophys. Res. Lett.* **2021**, *48*, e2021GL094143. [CrossRef] [PubMed]
7. McCollom, T.M.; Klein, F.; Ramba, M. Hydrogen generation from serpentinization of iron-rich olivine on Mars, icy moons, and other planetary bodies. *Icarus* **2022**, *372*, 114754. [CrossRef]
8. Nathues, A.; Hoffmann, M.; Cloutis, E.A.; Schäfer, M.; Reddy, V.; Christensen, U.; Sierks, H.; Thangjam, G.S.; Le Corre, L.; Mengel, K.; et al. Detection of serpentine in exogenic carbonaceous chondrite material on Vesta from Dawn FC data. *Icarus* **2014**, *239*, 222–237. [CrossRef]
9. Zega, T.J.; Garvie, L.A.J.; Dódony, I.; Friedrich, H.; Stroud, R.M.; Buseck, P.R. Polyhedral serpentine grains in CM chondrites. *Meteorit. Planet. Sci.* **2006**, *41*, 681–688. [CrossRef]
10. Thayer, T.P. Serpentinization considered as a constant-volume metasomatic process. *Am. Mineral. J. Earth Planet. Mater.* **1966**, *51*, 685–710.
11. Neubeck, A.; Duc, N.T.; Bastviken, D.; Crill, P.; Holm, N.G. Formation of H_2 and CH_4 by weathering of olivine at temperatures between 30 and 70 °C. *Geochem. Trans.* **2011**, *12*, 1–10. [CrossRef]
12. McCollom, T.M.; Donaldson, C. Generation of hydrogen and methane during experimental low-temperature reaction of ultramafic rocks with water. *Astrobiology* **2016**, *16*, 389–406. [CrossRef]
13. Leong, J.A.M.; Shock, E.L. Thermodynamic constraints on the geochemistry of low-temperature, continental, serpentinization-generated fluids. *Am. J. Sci.* **2020**, *320*, 185–235. [CrossRef]
14. Storch, H.H. *The Fischer-Tropsch and Related Syntheses, Including a Summary of Theoretical and Applied Contact Catalysis*; Storch, H.H., Golumbic, N., Anderson, R.B., Eds.; Wiley: Hoboken, NJ, USA, 1951.
15. McCollom, T.M.; Seewald, J.S. A reassessment of the potential for reduction of dissolved CO_2 to hydrocarbons during serpentinization of olivine. *Geochim. Cosmochim. Acta* **2001**, *65*, 3769–3778. [CrossRef]
16. McCollom, T.M.; Seewald, J.S. Serpentinites, Hydrogen, and Life. *Elements* **2013**, *9*, 129–134. [CrossRef]
17. McCollom, T.M.; Seewald, J.S.; German, C.R. Investigation of extractable organic compounds in deep-sea hydrothermal vent fluids along the Mid-Atlantic Ridge. *Geochim. Cosmochim. Acta* **2015**, *156*, 122–144. [CrossRef]
18. Alexander, C.M.O.; Fogel, M.; Yabuta, H.; Cody, G.D. The origin and evolution of chondrites recorded in the elemental and isotopic compositions of their macromolecular organic matter. *Geochim. Cosmochim. Acta* **2007**, *71*, 4380–4403. [CrossRef]
19. Pearce, B.K.D.; Pudritz, R.E. Seeding the pregenetic Earth: Meteoritic abundances of nucleobases and potential reaction pathways. *Astrophys. J.* **2015**, *807*, 85. [CrossRef]

20. Oze, C.; Sharma, M. Have olivine, will gas: Serpentinization and the abiogenic production of methane on Mars. *Geophys. Res. Lett.* **2005**, *32*. [CrossRef]
21. Lodders, K. A survey of shergottite, nakhlite and chassigny meteorites whole-rock compositions. *Meteorit. Planet. Sci.* **1998**, *33*, A183–A190. [CrossRef]
22. Zolensky, M.; Barrett, R.; Browning, L. Mineralogy and composition of matrix and chondrule rims in carbonaceous chondrites. *Geochim. Cosmochim. Acta* **1993**, *57*, 3123–3148. [CrossRef]
23. Brearley, A.J. The action of water. *Meteor. Early Sol. Syst. II* **2006**, *943*, 587–624.
24. Velbel, M.A.; Palmer, E.E. Fine-grained serpentine in CM2 carbonaceous chondrites and its implications for the extent of aqueous alteration on the parent body: A review. *Clays Clay Miner.* **2011**, *59*, 416–432. [CrossRef]
25. Velbel, M.A.; Tonui, E.K.; Zolensky, M.E. Replacement of olivine by serpentine in the carbonaceous chondrite Nogoya (CM2). *Geochim. Cosmochim. Acta* **2012**, *87*, 117–135. [CrossRef]
26. Gyollai, I.; Chatzitheodoridis, E.; Kereszturi, Á.; Szabó, M. Multiple generation magmatic and hydrothermal processes in a Martian subvolcanic environment based on the analysis of Yamato-000593 nakhlite meteorite. *Meteorit. Planet. Sci.* **2023**, *58*, 218–240. [CrossRef]
27. Farley, K.A.; Stack, K.M.; Shuster, D.L.; Horgan, B.H.N.; Hurowitz, J.A.; Tarnas, J.D.; Simon, J.I.; Sun, V.Z.; Scheller, E.L.; Moore, K.R.; et al. Aqueously altered igneous rocks sampled on the floor of Jezero crater, Mars. *Science* **2022**, *377*, eabo2196. [CrossRef]
28. Liu, Y.; Tice, M.M.; Schmidt, M.E.; Treiman, A.H.; Kizovski, T.V.; Hurowitz, J.A.; Allwood, A.C.; Henneke, J.; Pedersen, D.A.K.; VanBommel, S.J.; et al. An olivine cumulate outcrop on the floor of Jezero crater, Mars. *Science* **2022**, *377*, 1513–1519. [CrossRef]
29. Wiens, R.C.; Udry, A.; Beyssac, O.; Quantin-Nataf, C.; Mangold, N.; Cousin, A.; Mandon, L.; Bosak, T.; Forni, O.; McLennan, S.M.; et al. Compositionally and density stratified igneous terrain in Jezero crater, Mars. *Sci. Adv.* **2022**, *8*, eabo3399. [CrossRef]
30. Clark, B.C.; Van Hart, D.C. The salts of Mars. *Icarus* **1981**, *45*, 370–378. [CrossRef]
31. Hoffert, M.I.; Callegari, A.J.; Hsieh, C.T.; Ziegler, W. Liquid water on Mars: An energy balance climate model for CO_2/H_2O atmospheres. *Icarus* **1981**, *47*, 112–129. [CrossRef]
32. Brakenridge, G.R.; Newsom, H.E.; Baker, V.R. Ancient hot springs on Mars: Origins and paleoenvironmental significance of small Martian valleys. *Geology* **1985**, *13*, 859–862. [CrossRef]
33. Lucchitta, B.K. Valles Marineris, Mars: Wet debris flows and ground ice. *Icarus* **1987**, *72*, 411–429. [CrossRef]
34. Malin, M.C.; Edgett, K.S. Evidence for recent groundwater seepage and surface runoff on Mars. *Science* **2000**, *288*, 2330–2335. [CrossRef]
35. Knauth, L.P.; Burt, D.M. Eutectic brines on Mars: Origin and possible relation to young seepage features. *Icarus* **2002**, *158*, 267–271. [CrossRef]
36. Hecht, M.H.; Kounaves, S.P.; Quinn, R.C.; West, S.J.; Young, S.M.M.; Ming, D.W.; Catling, D.C.; Clark, B.C.; Boynton, W.V.; Hoffman, J.; et al. Detection of perchlorate and the soluble chemistry of martian soil at the Phoenix lander site. *Science* **2009**, *325*, 64–67. [CrossRef]
37. Möhlmann, D.; Thomsen, K. Properties of cryobrines on Mars. *Icarus* **2011**, *212*, 123–130. [CrossRef]
38. Chevrier, V.F.; Rivera-Valentin, E.G. Formation of recurring slope lineae by liquid brines on present-day Mars. *Geophys. Res. Lett.* **2012**, *39*. [CrossRef]
39. Michalski, J.R.; Cuadros, J.; Niles, P.B.; Parnell, J.; Rogers, A.D.; Wright, S.P. Groundwater activity on Mars and implications for a deep biosphere. *Nat. Geosci.* **2013**, *6*, 133–138. [CrossRef]
40. Rampe, E.; Ming, D.; Blake, D.; Bristow, T.; Chipera, S.; Grotzinger, J.; Morris, R.; Morrison, S.; Vaniman, D.; Yen, A.; et al. Mineralogy of an ancient lacustrine mudstone succession from the Murray formation, Gale crater, Mars. *Earth Planet. Sci. Lett.* **2017**, *471*, 172–185. [CrossRef]
41. Salese, F.; Pondrelli, M.; Neeseman, A.; Schmidt, G.; Ori, G.G. Geological evidence of planet-wide groundwater system on mars. *J. Geophys. Res. Planets* **2019**, *124*, 374–395. [CrossRef]
42. Chevrier, V.F.; Rivera-Valentín, E.G.; Soto, A.; Altheide, T.S. Global temporal and geographic stability of brines on present-day Mars. *Planet. Sci. J.* **2020**, *1*, 64. [CrossRef]
43. Chevrier, V.F.; Fitting, A.B.; Rivera-Valentín, E.G. Limited stability of multicomponent brines on the surface of Mars. *Planet. Sci. J.* **2022**, *3*, 125. [CrossRef]
44. Mangold, N.; Poulet, F.; Mustard, J.F.; Bibring, J.; Gondet, B.; Langevin, Y.; Ansan, V.; Masson, P.; Fassett, C.; Head, J.W.; et al. Mineralogy of the Nili Fossae region with OMEGA/Mars Express data: 2. Aqueous alteration of the crust. *J. Geophys. Res. Planets* **2007**, *112*, E08S04. [CrossRef]
45. Bishop, J.L.; McKeown, N.K.; Noe Dobrea, E.Z.; Ehlmann, B.L.; Michalski, J.R.; Milliken, R.E.; Poulet, F.; Mustard, J.F.; Swayze, G.; Murchie, S.L. Phyllosilicate diversity observed by CRISM in Mawrth Vallis: Identification of nontronite, mont-morillonite, kaolinite, and hydrated silica. In Proceedings of the 39th Annual Lunar and Planetary Science Conference, League City, TX, USA, 10–14 March 2008; p. 2124.
46. Ehlmann, B.L.; Mustard, J.F.; Murchie, S.L. Geologic setting of serpentine deposits on Mars. *Geophys. Res. Lett.* **2010**, *37*. [CrossRef]
47. Milliken, R.E.; Grotzinger, J.P.; Thomson, B.J. Paleoclimate of Mars as captured by the stratigraphic record in Gale Crater. *Geophys. Res. Lett.* **2010**, *37*. [CrossRef]

48. Wiseman, S.M.; Arvidson, R.E.; Morris, R.V.; Poulet, F.; Andrews-Hanna, J.C.; Bishop, J.L.; Murchie, S.L.; Seelos, F.P.; Marais, D.D.; Griffes, J.L. Spectral and stratigraphic mapping of hydrated sulfate and phyllosilicate-bearing deposits in northern Sinus Meridiani, Mars. *J. Geophys. Res.* **2010**, *115*. [CrossRef]
49. Bultel, B.; Quantin-Nataf, C.; Andréani, M.; Clénet, H.; Lozac'h, L. Deep alteration between Hellas and Isidis basins. *Icarus* **2015**, *260*, 141–160. [CrossRef]
50. Amador, E.S.; Bandfield, J.L.; Thomas, N.H. A search for minerals associated with serpentinization across Mars using CRISM spectral data. *Icarus* **2018**, *311*, 113–134. [CrossRef]
51. Tarnas, J.D.; Mustard, J.F.; Lin, H.; Goudge, T.A.; Amador, E.S.; Bramble, M.S.; Kremer, C.H.; Zhang, X.; Itoh, Y.; Parente, M. Orbital identification of hydrated silica in Jezero crater, Mars. *Geophys. Res. Lett.* **2019**, *46*, 12771–12782. [CrossRef]
52. Horgan, B.H.; Anderson, R.B.; Dromart, G.; Amador, E.S.; Rice, M.S. The mineral diversity of Jezero crater: Evidence for possible lacustrine carbonates on Mars. *Icarus* **2020**, *339*, 113526. [CrossRef]
53. Lin, H.; Tarnas, J.; Mustard, J.; Zhang, X.; Wei, Y.; Wan, W.; Klein, F.; Kellner, J. Dynamic aperture factor analysis/target transformation (DAFA/TT) for Mg-serpentine and Mg-carbonate mapping on Mars with CRISM near-infrared data. *Icarus* **2021**, *355*, 114168. [CrossRef]
54. Schulte, M.; Blake, D.; Hoehler, T.M.; McCollom, T.M.; Donaldson, C.; Saladino, R.; Botta, G.; Bizzarri, B.M.; Di Mauro, E.; Ruiz, J.M.G.; et al. Serpentinization and Its Implications for Life on the Early Earth and Mars. *Astrobiology* **2006**, *6*, 364–376. [CrossRef]
55. Atreya, S.K.; Mahaffy, P.R.; Wong, A.-S. Methane and related trace species on Mars: Origin, loss, implications for life, and habitability. *Planet. Space Sci.* **2007**, *55*, 358–369. [CrossRef]
56. Sherwood Lollar, B.; Voglesonger, K.; Lin, L.; Lacrampe-Couloume, G.; Telling, J.; Abrajano, T.A.; Onstott, T.C.; Pratt, L.M. Hydrogeologic controls on episodic H2 release from Precambrian fractured rocks—Energy for deep subsurface life on Earth and Mars. *Astrobiology* **2007**, *7*, 971–986. [CrossRef]
57. Stamenkovic, V.; Lynch, K.; Boston, P.; Tarnas, J.; Edwards, C.D.; Sherwood-Lollar, B.; Atreya, S.; Templeton, A.; Freeman, A.; Fischer, W.; et al. Deep Trek: Science of Subsurface Habitability & Life on Mars. *Bull. AAS* **2021**, *53*, 250. [CrossRef]
58. Hoefen, T.M.; Clark, R.N.; Bandfield, J.L.; Smith, M.D.; Pearl, J.C.; Christensen, P.R. Discovery of Olivine in the Nili Fossae Region of Mars. *Science* **2003**, *302*, 627–630. [CrossRef] [PubMed]
59. Christensen, P.R.; Bandfield, J.L.; Hamilton, V.E.; Ruff, S.W.; Kieffer, H.H.; Titus, T.N.; Malin, M.C.; Morris, R.V.; Lane, M.D.; Clark, R.L.; et al. Mars Global Surveyor Thermal Emission Spectrometer experiment: Investigation description and surface science results. *J. Geophys. Res. Planets* **2001**, *106*, 23823–23871. [CrossRef]
60. Mustard, J.F.; Poulet, F.; Gendrin, A.; Bibring, J.-P.; Langevin, Y.; Gondet, B.; Mangold, N.; Bellucci, G.; Altieri, F. Olivine and Pyroxene Diversity in the Crust of Mars. *Science* **2005**, *307*, 1594–1597. [CrossRef]
61. Mustard, J.F.; Poulet, F.; Head, J.W.; Mangold, N.; Bibring, J.; Pelkey, S.M.; Fassett, C.I.; Langevin, Y.; Neukum, G. Mineralogy of the Nili Fossae region with OMEGA/Mars Express data: 1. Ancient impact melt in the Isidis Basin and implications for the transition from the Noachian to Hesperian. *J. Geophys. Res. Planets* **2007**, *112*. [CrossRef]
62. Bibring, J.-P.; Langevin, Y.; Gendrin, A.; Gondet, B.; Poulet, F.; Berthé, M.; Soufflot, A.; Arvidson, R.; Mangold, N.; Mustard, J.; et al. Mars Surface Diversity as Revealed by the OMEGA/Mars Express Observations. *Science* **2005**, *307*, 1576–1581. [CrossRef] [PubMed]
63. Brown, A.J.; Hook, S.J.; Baldridge, A.M.; Crowley, J.K.; Bridges, N.T.; Thomson, B.J.; Marion, G.M.; de Souza Filho, C.R.; Bishop, J.L. Hydrothermal formation of Clay-Carbonate alteration assemblages in the Nili Fossae region of Mars. *Earth Planet. Sci. Lett.* **2010**, *297*, 174–182. [CrossRef]
64. Viviano, C.E.; Moersch, J.E.; McSween, H.Y. Implications for early hydrothermal environments on Mars through the spectral evidence for carbonation and chloritization reactions in the Nili Fossae region. *J. Geophys. Res. Planets* **2013**, *118*, 1858–1872. [CrossRef]
65. Tutolo, B.M.; Tosca, N.J. Observational constraints on the process and products of Martian serpentinization. *Sci. Adv.* **2023**, *9*, eadd8472. [CrossRef]
66. Chevrier, V.F.; Morisson, M. Carbonate-Phyllosilicate Parageneses and Environments of Aqueous Alteration in Nili Fossae and Mars. *J. Geophys. Res. Planets* **2021**, *126*, e2020JE006698. [CrossRef]
67. Williford, K.H.; Farley, K.A.; Stack, K.M.; Allwood, A.C.; Beaty, D.; Beegle, L.W.; Bhartia, R.; Brown, A.J.; de la Torre Juarez, M.; Wiens, R.C.; et al. The NASA Mars 2020 rover mission and the search for extraterrestrial life. In *From Habitability to Life on Mars*; Elsevier: Amsterdam, The Netherlands, 2018; pp. 275–308.
68. Farley, K.A.; Williford, K.H.; Stack, K.M.; Bhartia, R.; Chen, A.; de la Torre, M.; Hand, K.; Goreva, Y.; Herd, C.D.K.; Hueso, R.; et al. Mars 2020 mission overview. *Space Sci. Rev.* **2020**, *216*, 1–41. [CrossRef]
69. Hyodo, R.; Usui, T. Searching for life on Mars and its moons. *Science* **2021**, *373*, 742. [CrossRef]
70. Bell, J.F., III; Maki, J.N.; Alwmark, S.; Ehlmann, B.L.; Fagents, S.A.; Grotzinger, J.P.; Gupta, S.; Hayes, A.; Herkenhoff, K.E.; Horgan, B.H.N.; et al. Geological, multispectral, and meteorological imaging results from the Mars 2020 Perseverance rover in Jezero crater. *Sci. Adv.* **2022**, *8*, eabo4856. [CrossRef]
71. Bishop, J.L.; Murad, E.; Lane, M.D.; Mancinelli, R.L. Multiple techniques for mineral identification on Mars: A study of hydrothermal rocks as potential analogues for astrobiology sites on Mars. *Icarus* **2004**, *169*, 311–323. [CrossRef]

72. Dartnell, L.R.; Desorgher, L.; Ward, J.M.; Coates, A.J. Modelling the surface and subsurface Martian radiation environment: Implications for astrobiology. *Geophys. Res. Lett.* **2007**, *34*. [CrossRef]
73. Levin, G.V.; Straat, P.A. The Case for Extant Life on Mars and Its Possible Detection by the Viking Labeled Release Experiment. *Astrobiology* **2016**, *16*, 798–810. [CrossRef]
74. Beaty, D.W.; Grady, M.M.; McSween, H.Y.; Sefton-Nash, E.; Carrier, B.L.; Altieri, F.; Amelin, Y.; Ammannito, E.; Anand, M.; Benning, L.G.; et al. The potential science and engineering value of samples delivered to Earth by Mars sample return: International MSR Objectives and Samples Team (iMOST). *Meteorit. Planet. Sci.* **2019**, *54*, S3–S152. [CrossRef]
75. Onstott, T.; Ehlmann, B.; Sapers, H.; Coleman, M.; Ivarsson, M.; Marlow, J.; Neubeck, A.; Niles, P. Paleo-rock-hosted life on Earth and the search on Mars: A review and strategy for exploration. *Astrobiology* **2019**, *19*, 1230–1262. [CrossRef] [PubMed]
76. Tarnas, J.; Mustard, J.; Lollar, B.S.; Stamenković, V.; Cannon, K.; Lorand, J.-P.; Onstott, T.; Michalski, J.; Warr, O.; Palumbo, A.; et al. Earth-like Habitable Environments in the Subsurface of Mars. *Astrobiology* **2021**, *21*, 741–756. [CrossRef] [PubMed]
77. Brown, A.J.; Kah, L.; Mandon, L.; Wiens, R.; Pinet, P.; Clavé, E.; Mouélic, S.L.; Udry, A.; Gasda, P.J.; Royer, C.; et al. Properties of the Nili Fossae Olivine-clay-carbonate lithology: Orbital and in situ at Séítah. *arXiv* **2022**. [CrossRef]
78. Mustard, J.F.; Ehlmann, B.L.; Murchie, S.L.; Poulet, F.; Mangold, N.; Head, J.W.; Bibring, J.; Roach, L.H. Composition, Morphology, and Stratigraphy of Noachian Crust around the Isidis basin. *J. Geophys. Res. Planets* **2009**, *114*. [CrossRef]
79. Ehlmann, B.L.; Mustard, J.F.; Murchie, S.L.; Poulet, F.; Bishop, J.L.; Brown, A.J.; Calvin, W.M.; Clark, R.N.; Marais, D.J.D.; Milliken, R.E.; et al. Orbital Identification of Carbonate-Bearing Rocks on Mars. *Science* **2008**, *322*, 1828–1832. [CrossRef] [PubMed]
80. Fassett, C.I.; Head, J.W. Valley network-fed, open-basin lakes on Mars: Distribution and implications for Noachian surface and subsurface hydrology. *Icarus* **2008**, *198*, 37–56. [CrossRef]
81. Goudge, T.A.; Mustard, J.F.; Head, J.W.; Fassett, C.I.; Wiseman, S.M. Assessing the mineralogy of the watershed and fan deposits of the Jezero crater paleolake system, Mars. *J. Geophys. Res. Planets* **2015**, *120*, 775–808. [CrossRef]
82. Mangold, N. Intermittent warmth on young Mars. *Nat. Geosci.* **2021**, *14*, 112–113. [CrossRef]
83. Bethke, C.M. *Geochemical and Biogeochemical Reaction Modeling*, 3rd ed.; Cambridge University Press (CUP): Cambridge, UK, 2021; ISBN 9780511619670.
84. Helgeson, H.C. Evaluation of irreversible reactions in geochemical processes involving minerals and aqueous solutions—I. Thermodynamic relations. *Geochim. Cosmochim. Acta* **1968**, *32*, 853–877. [CrossRef]
85. Helgeson, H.C.; Garrels, R.M.; MacKenzie, F.T. Evaluation of irreversible reactions in geochemical processes involving minerals and aqueous solutions—II. Applications. *Geochim. Cosmochim. Acta* **1969**, *33*, 455–481. [CrossRef]
86. Griffith, L.L.; Shock, E.L. A geochemical model for the formation of hydrothermal carbonates on Mars. *Nature* **1995**, *377*, 406–408. [CrossRef]
87. Griffith, L.L.; Shock, E.L. Hydrothermal hydration of Martian crust: Illustration via geochemical model calculations. *J. Geophys. Res. Planets* **1997**, *102*, 9135–9143. [CrossRef]
88. Jones, C.L.; Brearley, A.J. Experimental aqueous alteration of the Allende meteorite under oxidizing conditions: Constraints on asteroidal alteration. *Geochim. Cosmochim. Acta* **2006**, *70*, 1040–1058. [CrossRef]
89. McAdam, A.C.; Zolotov, M.Y.; Mironenko, M.V.; Sharp, T.G. Formation of silica by low-temperature acid alteration of Martian rocks: Physical-chemical constraints. *J. Geophys. Res. Planets* **2008**, *113*. [CrossRef]
90. Bouquet, A.; Glein, C.R.; Wyrick, D.; Waite, J.H. Alternative Energy: Production of H_2 by Radiolysis of Water in the Rocky Cores of Icy Bodies. *Astrophys. J.* **2017**, *840*, L8. [CrossRef]
91. Castillo-Rogez, J.; Neveu, M.; McSween, H.Y.; Fu, R.R.; Toplis, M.J.; Prettyman, T. Insights into Ceres's evolution from surface composition. *Meteorit. Planet. Sci.* **2018**, *53*, 1820–1843. [CrossRef]
92. Glein, C.R.; Waite, J.R. The Carbonate Geochemistry of Enceladus' Ocean. *Geophys. Res. Lett.* **2020**, *47*, e2019GL085885. [CrossRef]
93. Bouquet, A.; Miller, K.E.; Glein, C.R.; Mousis, O. Limits on the contribution of early endogenous radiolysis to oxidation in carbonaceous chondrites' parent bodies. *Astron. Astrophys.* **2021**, *653*, A59. [CrossRef]
94. Ray, C.; Glein, C.R.; Waite, J.H.; Teolis, B.; Hoehler, T.; Huber, J.A.; Lunine, J.; Postberg, F. Oxidation processes diversify the metabolic menu on Enceladus. *Icarus* **2021**, *364*, 114248. [CrossRef]
95. Oelkers, E.H.; Bénézeth, P.; Pokrovski, G.S. Thermodynamic databases for water-rock interaction. *Rev. Miner. Geochem.* **2009**, *70*, 1–46. [CrossRef]
96. Osinski, G.R.; Tornabene, L.L.; Banerjee, N.R.; Cockell, C.S.; Flemming, R.; Izawa, M.R.; McCutcheon, J.; Parnell, J.; Preston, L.J.; Pickersgill, A.E. Im-pact-generated hydrothermal systems on Earth and Mars. *Icarus* **2013**, *224*, 347–363. [CrossRef]
97. Rapin, W.; Meslin, P.-Y.; Maurice, S.; Vaniman, D.; Nachon, M.; Mangold, N.; Schröder, S.; Gasnault, O.; Forni, O.; Wiens, R.; et al. Hydration state of calcium sulfates in Gale crater, Mars: Identification of bassanite veins. *Earth Planet. Sci. Lett.* **2016**, *452*, 197–205. [CrossRef]
98. Yen, A.; Ming, D.; Vaniman, D.; Gellert, R.; Blake, D.; Morris, R.; Morrison, S.; Bristow, T.; Chipera, S.; Edgett, K.; et al. Multiple stages of aqueous alteration along fractures in mudstone and sandstone strata in Gale Crater, Mars. *Earth Planet. Sci. Lett.* **2017**, *471*, 186–198. [CrossRef]
99. Nachon, M.; Mangold, N.; Forni, O.; Kah, L.; Cousin, A.; Wiens, R.; Anderson, R.; Blaney, D.; Blank, J.; Calef, F.; et al. Chemistry of diagenetic features analyzed by ChemCam at Pahrump Hills, Gale crater, Mars. *Icarus* **2017**, *281*, 121–136. [CrossRef]

100. L'Haridon, J.; Mangold, N.; Meslin, P.-Y.; Johnson, J.; Rapin, W.; Forni, O.; Cousin, A.; Payré, V.; Dehouck, E.; Nachon, M.; et al. Chemical variability in mineralized veins observed by ChemCam on the lower slopes of Mount Sharp in Gale crater, Mars. *Icarus* **2018**, *311*, 69–86. [CrossRef]
101. Tosca, N.J.; McLennan, S.M.; Dyar, M.D.; Sklute, E.C.; Michel, F.M. Fe oxidation processes at Meridiani Planum and implications for secondary Fe mineralogy on Mars. *J. Geophys. Res. Planets* **2008**, *113*. [CrossRef]
102. Sheppard, R.Y.; Thorpe, M.T.; Fraeman, A.A.; Fox, V.K.; Milliken, R.E. Merging perspectives on secondary minerals on mars: A review of ancient water-rock interactions in gale crater inferred from orbital and in-situ observations. *Minerals* **2021**, *11*, 986. [CrossRef]
103. Toner, J.; Catling, D.; Light, B. The formation of supercooled brines, viscous liquids, and low-temperature perchlorate glasses in aqueous solutions relevant to Mars. *Icarus* **2014**, *233*, 36–47. [CrossRef]
104. Toner, J.; Catling, D.; Light, B. Soluble salts at the Phoenix Lander site, Mars: A reanalysis of the Wet Chemistry Laboratory data. *Geochim. Cosmochim. Acta* **2014**, *136*, 142–168. [CrossRef]
105. Toner, J.D.; Catling, D.C.; Light, B. Modeling salt precipitation from brines on Mars: Evaporation versus freezing origin for soil salts. *Icarus* **2015**, *250*, 451–461. [CrossRef]
106. McEwen, A.S.; Ojha, L.; Dundas, C.M.; Mattson, S.S.; Byrne, S.; Wray, J.J.; Cull, S.C.; Murchie, S.L.; Thomas, N.; Gulick, V.C. Seasonal Flows on Warm Martian Slopes. *Science* **2011**, *333*, 740–743. [CrossRef]
107. Hassler, D.M.; Zeitlin, C.; Wimmer-Schweingruber, R.F.; Ehresmann, B.; Rafkin, S.; Eigenbrode, J.L.; Brinza, D.E.; Weigle, G.; Böttcher, S.; Böhm, E.; et al. Mars' surface radiation environment measured with the Mars Science Laboratory's Curiosity rover. *Science* **2014**, *343*, 1244797. [CrossRef]
108. Guo, J.; Zeitlin, C.; Wimmer-Schweingruber, R.F.; Hassler, D.M.; Posner, A.; Heber, B.; Köhler, J.; Rafkin, S.; Ehresmann, B.; Appel, J.K.; et al. Variations of dose rate observed by MSL/RAD in transit to Mars. *Astron. Astrophys.* **2015**, *577*, A58. [CrossRef]
109. Hamilton, V.E.; Christensen, P.R. Evidence for extensive, olivine-rich bedrock on Mars. *Geology* **2005**, *33*, 433. [CrossRef]
110. Koeppen, W.C.; Hamilton, V.E. Global distribution, composition, and abundance of olivine on the surface of Mars from thermal infrared data. *J. Geophys. Res. Planets* **2008**, *113*. [CrossRef]
111. Ody, A.; Poulet, F.; Bibring, J.; Loizeau, D.; Carter, J.; Gondet, B.; Langevin, Y. Global investigation of olivine on Mars: Insights into crust and mantle compositions. *J. Geophys. Res. Planets* **2013**, *118*, 234–262. [CrossRef]
112. Kremer, C.H.; Mustard, J.F.; Bramble, M.S. A widespread olivine-rich ash deposit on Mars. *Geology* **2019**, *47*, 677–681. [CrossRef]
113. Brown, A.J.; Viviano, C.E.; Goudge, T.A. Olivine-Carbonate Mineralogy of the Jezero Crater Region. *J. Geophys. Res. Planets* **2020**, *125*, e2019JE006011. [CrossRef]
114. Ruff, S.W.; Hamilton, V.E.; Rogers, A.D.; Edwards, C.S.; Horgan, B.H. Olivine and carbonate-rich bedrock in Gusev crater and the Nili Fossae region of Mars may be altered ignimbrite deposits. *Icarus* **2022**, *380*, 114974. [CrossRef]
115. Poulet, F.; Mangold, N.; Platevoet, B.; Bardintzeff, J.-M.; Sautter, V.; Mustard, J.; Bibring, J.-P.; Pinet, P.; Langevin, Y.; Gondet, B.; et al. Quantitative compositional analysis of Martian mafic regions using the MEx/OMEGA reflectance data: 2. Petrological impli-cations. *Icarus* **2009**, *201*, 84–101. [CrossRef]
116. Mandon, L.; Quantin-Nataf, C.; Thollot, P.; Mangold, N.; Lozac'H, L.; Dromart, G.; Beck, P.; Dehouck, E.; Breton, S.; Millot, C.; et al. Refining the age, emplacement and alteration scenarios of the olivine-rich unit in the Nili Fossae region, Mars. *Icarus* **2020**, *336*, 113436. [CrossRef]
117. Borg, L.E.; Nyquist, L.E.; Wiesmann, H.; Reese, Y. Constraints on the petrogenesis of Martian meteorites from the Rb-Sr and Sm-Nd isotopic systematics of the lherzolitic shergottites ALH77005 and LEW88516. *Geochim. Cosmochim. Acta* **2002**, *66*, 2037–2053. [CrossRef]
118. Mangold, N.; Dromart, G.; Ansan, V.; Salese, F.; Kleinhans, M.G.; Massé, M.; Quantin-Nataf, C.; Stack, K.M. Fluvial Regimes, Morphometry, and Age of Jezero Crater Paleolake Inlet Valleys and Their Exobiological Significance for the 2020 Rover Mission Landing Site. *Astrobiology* **2020**, *20*, 994–1013. [CrossRef] [PubMed]
119. Borg, L.E.; Nyquist, L.E.; Wiesmann, H.; Shih, C.-Y.; Reese, Y. The age of Dar al Gani 476 and the differentiation history of the martian meteorites inferred from their radiogenic isotopic systematics. *Geochim. Cosmochim. Acta* **2003**, *67*, 3519–3536. [CrossRef]
120. Nyquist, L.; Bogard, D.; Shih, C.-Y.; Park, J.; Reese, Y.; Irving, A. Concordant Rb–Sr, Sm–Nd, and Ar–Ar ages for Northwest Africa 1460: A 346Ma old basaltic shergottite related to "lherzolitic" shergottites. *Geochim. Cosmochim. Acta* **2009**, *73*, 4288–4309. [CrossRef]
121. Brennecka, G.A.; Borg, L.E.; Wadhwa, M. Insights into the Martian mantle: The age and isotopics of the meteorite fall Tissint. *Meteorit. Planet. Sci.* **2014**, *49*, 412–418. [CrossRef]
122. Cohen, B.E.; Mark, D.F.; Cassata, W.S.; Lee, M.R.; Tomkinson, T.; Smith, C.L. Taking the pulse of Mars via dating of a plume-fed volcano. *Nat. Commun.* **2017**, *8*, 640–649. [CrossRef]
123. Herd, C.D.; Walton, E.L.; Agee, C.B.; Muttik, N.; Ziegler, K.; Shearer, C.K.; Bell, A.S.; Santos, A.R.; Burger, P.V.; Simon, J.I.; et al. The Northwest Africa 8159 martian meteorite: Expanding the martian sample suite to the early Amazonian. *Geochim. Cosmochim. Acta* **2017**, *218*, 1–26. [CrossRef]
124. Lapen, T.J.; Righter, M.; Andreasen, R.; Irving, A.J.; Satkoski, A.M.; Beard, B.L.; Nishiizumi, K.; Jull, A.J.T.; Caffee, M.W. Two billion years of magmatism recorded from a single Mars meteorite ejection site. *Sci. Adv.* **2017**, *3*, e1600922. [CrossRef]
125. Udry, A.; Howarth, G.H.; Herd, C.D.K.; Day, J.M.D.; Lapen, T.J.; Filiberto, J. *What Martian Meteorites Reveal about the Interior and Surface of Mars*; Blackwell Publishing Ltd.: Hoboken, NJ, USA, 2020. [CrossRef]

126. Varnes, E.S.; Jakosky, B.M.; McCollom, T.M. Biological potential of Martian hydrothermal systems. *Astrobiology* **2003**, *3*, 407–414. [CrossRef]
127. Tosca, N.; McLennan, S.; Clark, B.; Grotzinger, J.; Hurowitz, J.; Knoll, A.; Schröder, C.; Squyres, S. Geochemical modeling of evaporation processes on Mars: Insight from the sedimentary record at Meridiani Planum. *Earth Planet. Sci. Lett.* **2005**, *240*, 122–148. [CrossRef]
128. Bridges, J.; Schwenzer, S. The nakhlite hydrothermal brine on Mars. *Earth Planet. Sci. Lett.* **2012**, *359–360*, 117–123. [CrossRef]
129. Ramkissoon, N.K.; Turner, S.M.R.; Macey, M.C.; Schwenzer, S.P.; Reed, M.H.; Pearson, V.K.; Olsson-Francis, K. Exploring the environments of Martian impact-generated hydrothermal systems and their potential to support life. *Meteorit. Planet. Sci.* **2021**, *56*, 1350–1368. [CrossRef]
130. Chevrier, V.F.; Hanley, J.; Altheide, T.S. Stability of perchlorate hydrates and their liquid solutions at the Phoenix landing site, Mars. *Geophys. Res. Lett.* **2009**, *36*. [CrossRef]
131. Primm, K.; Gough, R.; Chevrier, V.; Tolbert, M. Freezing of perchlorate and chloride brines under Mars-relevant conditions. *Geochim. Cosmochim. Acta* **2017**, *212*, 211–220. [CrossRef]
132. Boynton, W.V.; Ming, D.W.; Kounaves, S.P.; Young, S.M.M.; Arvidson, R.E.; Hecht, M.H.; Hoffman, J.; Niles, P.B.; Hamara, D.K.; Quinn, R.C.; et al. Evidence for calcium carbonate at the Mars Phoenix landing site. *Science* **2009**, *325*, 61–64. [CrossRef]
133. Cull, S.C.; Arvidson, R.E.; Catalano, J.G.; Ming, D.W.; Morris, R.V.; Mellon, M.T.; Lemmon, M. Concentrated perchlorate at the Mars Phoenix landing site: Evidence for thin film liquid water on Mars. *Geophys. Res. Lett.* **2010**, *37*. [CrossRef]
134. Orosei, R.; Lauro, S.E.; Pettinelli, E.; Cicchetti, A.; Coradini, M.; Cosciotti, B.; Di Paolo, F.; Flamini, E.; Mattei, E.; Pajola, M.; et al. Radar evidence of subglacial liquid water on Mars. *Science* **2018**, *361*, 490–493. [CrossRef]
135. Rivera-Valentín, E.G.; Chevrier, V.F.; Soto, A.; Martínez, G. Distribution and habitability of (meta)stable brines on present-day Mars. *Nat. Astron.* **2020**, *4*, 756–761. [CrossRef]
136. Cone, K.A.; Palin, R.M.; Singha, K. Unsupervised machine learning with petrological database ApolloBasaltDB reveals complexity in lunar basalt major element oxide and mineral distribution patterns. *Icarus* **2020**, *346*, 113787. [CrossRef]
137. Hallsworth, J.E. Salt deliquescence can support extraterrestrial life. *Nat. Astron.* **2020**, *4*, 739–740. [CrossRef]
138. Coates, J.D.; Achenbach, L.A. Microbial perchlorate reduction: Rocket-fuelled metabolism. *Nat. Rev. Microbiol.* **2004**, *2*, 569–580. [CrossRef]
139. Góbi, S.; Kereszturi, Á. Analyzing the role of interfacial water on sulfate formation on present Mars. *Icarus* **2019**, *322*, 135–143. [CrossRef]
140. Marion, G.; Catling, D.; Zahnle, K.; Claire, M. Modeling aqueous perchlorate chemistries with applications to Mars. *Icarus* **2010**, *207*, 675–685. [CrossRef]
141. De Pater, I.; Lissauer, J.J. *Planetary Sciences*; Cambridge University Press: Cambridge, UK, 2015.
142. Scealy, J.L.; de Caritat, P.; Grunsky, E.C.; Tsagris, M.T.; Welsh, A.H. Robust Principal Component Analysis for Power Transformed Compositional Data. *J. Am. Stat. Assoc.* **2015**, *110*, 136–148. [CrossRef]
143. Nazarpour, A.; Omran, N.R.; Paydar, G.R.; Sadeghi, B.; Matroud, F.; Nejad, A.M. Application of classical statistics, logratio transformation and multifractal approaches to delineate geochemical anomalies in the Zarshuran gold district, NW Iran. *Geochemistry* **2015**, *75*, 117–132. [CrossRef]
144. Chen, D.; Wei, J.; Wang, W.; Shi, W.; Li, H.; Zhan, X. Comparison of Methods for Determining the Thresholds of Geochemical Anomalies and the Prospecting Direction—A Case of Gold Deposits in the Gouli Exploration Area, Qinghai Province. *Minerals* **2019**, *9*, 368. [CrossRef]
145. Jansson, N.F.; Allen, R.L.; Skogsmo, G.; Tavakoli, S. Principal component analysis and K-means clustering as tools during exploration for Zn skarn deposits and industrial carbonates, Sala area, Sweden. *J. Geochem. Explor.* **2022**, *233*, 106909. [CrossRef]
146. Soares, M.F.; Timm, L.C.; Siqueira, T.M.; dos Santos, R.C.V.; Reichardt, K. Assessing the spatial variability of saturated soil hydraulic conductivity at the watershed scale using the sequential Gaussian co-simulation method. *CATENA* **2023**, *221*, 106756. [CrossRef]
147. McKillup, S.; Dyar, M.D. *Geostatistics Explained*; Cambridge University Press (CUP): Cambridge, UK, 2010; ISBN 9780511807558.
148. Amend, J.P.; Shock, E.L. Energetics of overall metabolic reactions of thermophilic and hyperthermophilic Archaea and Bacteria. *FEMS Microbiol. Rev.* **2001**, *25*, 175–243. [CrossRef]
149. Cardace, D.; Meyer-Dombard, D.R.; Woycheese, K.M.; Arcilla, C.A. Feasible metabolisms in high pH springs of the Philippines. *Front. Microbiol.* **2015**, *6*, 10. [CrossRef]
150. McCollom, T.M.; Donaldson, C.; Reveillaud, J.; Reddington, E.; McDermott, J.; Algar, C.; Meyer, J.L.; Sylva, S.; German, C.R.; Huber, J.A.; et al. Geochemical constraints on sources of metabolic energy for chemolithoautotrophy in ultramafic-hosted deep-sea hydrothermal systems. *Astrobiology* **2007**, *7*, 933–950. [CrossRef] [PubMed]
151. Canovas, P.A., III; Hoehler, T.; Shock, E.L. Geochemical bioenergetics during low-temperature serpentinization: An example from the Samail ophiolite, Sultanate of Oman. *J. Geophys. Res. Biogeosci.* **2017**, *122*, 1821–1847. [CrossRef]
152. Crespo-Medina, M.; Twing, K.I.; Sánchez-Murillo, R.; Brazelton, W.J.; McCollom, T.M.; Schrenk, M. Methane Dynamics in a Tropical Serpentinizing Environment: The Santa Elena Ophiolite, Costa Rica. *Front. Microbiol.* **2017**, *8*, 916. [CrossRef] [PubMed]
153. Cook, M.C.; Blank, J.G.; Suzuki, S.; Nealson, K.H.; Morrill, P.L. Assessing geochemical bioenergetics and microbial metabolisms at three terrestrial sites of serpentinization: The Tablelands (NL, CAN), The Cedars (CA, USA), and Aqua de Ney (CA, USA). *J. Geophys. Res. Biogeosci.* **2021**, *126*, e2019JG005542. [CrossRef]

154. Sabuda, M.C.; Putman, L.I.; Hoehler, T.M.; Kubo, M.D.; Brazelton, W.J.; Cardace, D.; Schrenk, M.O. Biogeochemical Gradients in a Serpentinization-Influenced Aquifer: Implications for Gas Exchange between the Subsurface and Atmosphere. *J. Geophys. Res. Biogeosci.* **2021**, *126*, e2020JG006209. [CrossRef]
155. Hazen, R.M.; Downs, R.T.; Morrison, S.M.; Tutolo, B.M.; Blake, D.F.; Bristow, T.F.; Chipera, S.J.; McSween, H.Y.; Ming, D.; Morris, R.V.; et al. On the diversity and formation modes of martian minerals. *J. Geophys. Res. Planets* **2023**, *128*, e2023JE007865. [CrossRef]
156. Oehler, D.Z.; Etiope, G. Methane Seepage on Mars: Where to Look and Why. *Astrobiology* **2017**, *17*, 1233–1264. [CrossRef]
157. Zolotov, M.Y.; Mironenko, M.V. Formation and fate of phyllosilicates on the surface of Mars: Geochemical modeling of aqueous weathering. In Proceedings of the Seventh International Conference on Mars, Pasadena, CA, USA, 9–13 July 2007; Volume 1353, p. 3365.
158. Webster, C.R.; Mahaffy, P.R.; Atreya, S.K.; Moores, J.E.; Flesch, G.J.; Malespin, C.; McKay, C.P.; Martinez, G.; Smith, C.L.; Martin-Torres, J.; et al. Background levels of methane in Mars' atmosphere show strong seasonal variations. *Science* **2018**, *360*, 1093–1096. [CrossRef]
159. Mumma, M.J.; Villanueva, G.L.; Novak, R.E.; Hewagama, T.; Bonev, B.P.; DiSanti, M.A.; Mandell, A.M.; Smith, M.D. Strong release of methane on Mars in northern summer 2003. *Science* **2009**, *323*, 1041–1045. [CrossRef]
160. Krasnopolsky, V.A.; Maillard, J.P.; Owen, T.C. Detection of methane in the martian atmosphere: Evidence for life? *Icarus* **2004**, *172*, 537–547. [CrossRef]
161. Amador, E.S.; Bandfield, J.L.; Brazelton, W.J.; Kelley, D.; Marshall, C.P.; Marshall, A.O.; Aitken, J.B.; Lai, B.; Vogt, S.; Breuer, P.; et al. The Lost City Hydrothermal Field: A Spectroscopic and Astrobiological Analogue for Nili Fossae, Mars. *Astrobiology* **2017**, *17*, 1138–1160. [CrossRef]
162. Thomas, N.H.; Bandfield, J.L. Identification and refinement of martian surface mineralogy using factor analysis and target transformation of near-infrared spectroscopic data. *Icarus* **2017**, *291*, 124–135. [CrossRef]
163. Hurowitz, J.A.; McLennan, S.M.; Tosca, N.J.; Arvidson, R.E.; Michalski, J.R.; Ming, D.W.; Schröder, C.; Squyres, S.W. In situ and experimental evidence for acidic weathering of rocks and soils on Mars. *J. Geophys. Res. Planets* **2006**, *111*. [CrossRef]
164. Schwenzer, S.P.; Kring, D.A. Impact-generated hydrothermal systems capable of forming phyllosilicates on Noachian Mars. *Geology* **2009**, *37*, 1091–1094. [CrossRef]
165. Tosca, N.J.; McLennan, S.M. Experimental constraints on the evaporation of partially oxidized acid-sulfate waters at the martian surface. *Geochim. Cosmochim. Acta* **2009**, *73*, 1205–1222. [CrossRef]
166. Marion, G.; Catling, D.; Crowley, J.; Kargel, J. Modeling hot spring chemistries with applications to martian silica formation. *Icarus* **2011**, *212*, 629–642. [CrossRef]
167. Filiberto, J.; Schwenzer, S.P. Alteration mineralogy of Home Plate and Columbia Hills—Formation conditions in context to impact, volcanism, and fluvial activity. *Meteorit. Planet. Sci.* **2013**, *48*, 1937–1957. [CrossRef]
168. Schwenzer, S.P.; Kring, D.A. Alteration minerals in impact-generated hydrothermal systems—Exploring host rock variability. *Icarus* **2013**, *226*, 487–496. [CrossRef]
169. Zolotov, M.Y.; Mironenko, M.V. Chemical models for martian weathering profiles: Insights into formation of layered phyllosilicate and sulfate deposits. *Icarus* **2016**, *275*, 203–220. [CrossRef]
170. Costello, L.J.; Filiberto, J.; Crandall, J.R.; Potter-McIntyre, S.L.; Schwenzer, S.P.; Miller, M.A.; Hummer, D.R.; Olsson-Francis, K.; Perl, S. Habitability of hydrothermal systems at Jezero and Gusev craters as constrained by hydrothermal alteration of a terrestrial mafic dike. *Geochemistry* **2020**, *80*, 125613. [CrossRef] [PubMed]
171. Macey, M.C.; Ramkissoon, N.K.; Cogliati, S.; Toubes-Rodrigo, M.; Stephens, B.P.; Kucukkilic-Stephens, E.; Schwenzer, S.P.; Pearson, V.K.; Preston, L.J.; Olsson-Francis, K. Habitability and Biosignature Formation in Simulated Martian Aqueous Environments. *Astrobiology* **2023**, *23*, 144–154. [CrossRef] [PubMed]
172. Bridges, J.; Catling, D.; Saxton, J.; Swindle, T.; Lyon, I.; Grady, M. Alteration assemblages in Martian meteorites: Implications for near-surface processes. *Space Sci. Rev.* **2001**, *96*, 365–392. [CrossRef]
173. Berger, G.; Meunier, A.; Beaufort, D. Clay mineral formation on Mars: Chemical constraints and possible contribution of basalt out-gassing. *Planet. Space Sci.* **2014**, *95*, 25–32. [CrossRef]
174. Catalano, J.G. Thermodynamic and mass balance constraints on iron-bearing phyllosilicate formation and alteration pathways on early Mars. *J. Geophys. Res. Planets* **2013**, *118*, 2124–2136. [CrossRef]
175. Ehlmann, B.L.; Mustard, J.F.; Swayze, G.A.; Clark, R.N.; Bishop, J.L.; Poulet, F.; Des Marais, L.H.; Roach, R.E.; Milliken, J.J.; Wray, O.; et al. Identification of hydrated silicate minerals on Mars using MRO-CRISM: Geologic context near Nili Fossae and implications for aqueous altera-tion. *J. Geophys. Res. Planets* **2009**, *114*. [CrossRef]
176. Ehlmann, B.L.; Mustard, J.F. An in-situ record of major environmental transitions on early Mars at Northeast Syrtis Major. *Geophys. Res. Lett.* **2012**, *39*. [CrossRef]
177. Carter, J.; Poulet, F.; Bibring, J.; Mangold, N.; Murchie, S. Hydrous minerals on Mars as seen by the CRISM and OMEGA imaging spectrometers: Updated global view. *J. Geophys. Res. Planets* **2013**, *118*, 831–858. [CrossRef]
178. Murchie, S.L.; Mustard, J.F.; Ehlmann, B.L.; Milliken, R.E.; Bishop, J.L.; McKeown, N.K.; Dobrea, E.Z.N.; Seelos, F.P.; Buczkowski, D.L.; Wiseman, S.M.; et al. A synthesis of Martian aqueous mineralogy after 1 Mars year of observations from the Mars Reconnaissance Orbiter. *J. Geophys. Res. Planets* **2009**, *114*. [CrossRef]

179. Ehlmann, B.L.; Mustard, J.F.; Clark, R.N.; Swayze, G.A.; Murchie, S.L. Evidence for low-grade metamorphism, hydrothermal alteration, and diagenesis on Mars from phyllosilicate mineral assemblages. *Clays Clay Miner.* **2011**, *59*, 359–377. [CrossRef]
180. Flahaut, J.; Quantin, C.; Clenet, H.; Allemand, P.; Mustard, J.F.; Thomas, P. Pristine Noachian crust and key geologic transitions in the lower walls of Valles Marineris: Insights into early igneous processes on Mars. *Icarus* **2012**, *221*, 420–435. [CrossRef]
181. Ehlmann, B.L.; Mustard, J.F.; Murchie, S.L.; Bibring, J.-P.; Meunier, A.; Fraeman, A.A.; Langevin, Y. Subsurface water and clay mineral formation during the early history of Mars. *Nature* **2011**, *479*, 53–60. [CrossRef] [PubMed]
182. Williams, K.B.; Sonzogni, Y.; Treiman, A.H. Amphibole in the Tissint Martian meteorite: Composition and implication for volatile content of parental magma. In Proceedings of the 45th Annual Lunar and Planetary Science Conference, Woodlands, TX, USA, 17–21 March 2014; p. 1435.
183. Vaniman, D.T.; Bish, D.L.; Ming, D.W.; Bristow, T.F.; Morris, R.V.; Blake, D.F.; Chipera, S.J.; Morrison, S.M.; Treiman, A.H.; Rampe, E.B.; et al. Mineralogy of a mudstone at Yellowknife Bay, Gale crater, Mars. *Science* **2014**, *343*, 1243480. [CrossRef] [PubMed]
184. Morris, R.V.; Klingelhöfer, G.; Schröder, C.; Fleischer, I.; Ming, D.W.; Yen, A.S.; Gellert, R.; Arvidson, R.E.; Rodionov, D.S.; Crumpler, L.S.; et al. Iron mineralogy and aqueous alteration from Husband Hill through Home Plate at Gusev crater, Mars: Results from the Mössbauer instrument on the Spirit Mars Exploration Rover. *J. Geophys. Res. Planets* **2008**, *113*. [CrossRef]
185. Christensen, P.R.; Bandfield, J.L.; Clark, R.N.; Edgett, K.S.; Hamilton, V.E.; Hoefen, T.; Kieffer, H.H.; Kuzmin, R.O.; Lane, M.D.; Malin, M.C.; et al. Detection of crystalline hematite mineralization on Mars by the Thermal Emission Spectrometer: Evidence for near-surface water. *J. Geophys. Res. Planets* **2000**, *105*, 9623–9642. [CrossRef]
186. Clark, B.; Morris, R.; McLennan, S.; Gellert, R.; Jolliff, B.; Knoll, A.; Squyres, S.; Lowenstein, T.; Ming, D.; Tosca, N.; et al. Chemistry and mineralogy of outcrops at Meridiani Planum. *Earth Planet. Sci. Lett.* **2005**, *240*, 73–94. [CrossRef]
187. Glotch, T.D.; Christensen, P.R.; Sharp, T.G. Fresnel modeling of hematite crystal surfaces and application to martian hematite spherules. *Icarus* **2006**, *181*, 408–418. [CrossRef]
188. Morris, R.V.; Klingelhoefer, G.; Schröder, C.; Rodionov, D.S.; Yen, A.; Ming, D.W.; de Souza, P.A., Jr.; Fleischer, I.; Wdowiak, T.; Gellert, R. Mössbauer mineralogy of rock, soil, and dust at Gusev crater, Mars: Spirit's journey through weakly altered olivine basalt on the plains and pervasively altered basalt in the Columbia Hills. *J. Geophys. Res. Planets* **2006**, *111*. [CrossRef]
189. McSween, H.Y., Jr.; Murchie, S.L.; Crisp, J.A.; Bridges, N.T.; Anderson, R.C.; Bell, J.F., III; Britt, D.T.; Brückner, J.; Dreibus, G.; Economou, T. Chemical, multispectral, and textural constraints on the composition and origin of rocks at the Mars Pathfinder landing site. *J. Geophys. Res. Planets* **1999**, *104*, 8679–8715. [CrossRef]
190. Squyres, S.W.; Arvidson, R.E.; Bell, J.F., III; Bruckner, J.; Cabrol, N.A.; Calvin, W.; Carr, M.H.; Christensen, P.R.; Clark, B.C.; Crumpler, L. The opportunity rover's Athena science investigation at Meridiani Planum, Mars. *Science* **2004**, *306*, 1698–1703. [CrossRef]
191. Squyres, S.W.; Grotzinger, J.P.; Arvidson, R.E.; Bell, J.F., III; Calvin, W.; Christensen, P.R.; Clark, B.C.; Crisp, J.A.; Farrand, W.H.; Herkenhoff, K.E. In situ evidence for an ancient aqueous environment at Meridiani Planum, Mars. *Science* **2004**, *306*, 1709–1714. [CrossRef]
192. Grotzinger, J.P.; Gupta, S.; Malin, M.C.; Rubin, D.M.; Schieber, J.; Siebach, K.; Sumner, D.Y.; Stack, K.M.; Vasavada, A.R.; Arvidson, R.E.; et al. Deposition, exhumation, and paleoclimate of an ancient lake deposit, Gale crater, Mars. *Science* **2015**, *350*, aac7575. [CrossRef] [PubMed]
193. Arvidson, R.E.; Anderson, R.C.; Haldemann, A.; Landis, G.A.; Li, R.; Lindemann, R.A.; Matijevic, J.R.; Morris, R.V.; Richter, L.; Squyres, S.W. Physical properties and localization investigations associated with the 2003 Mars Exploration rovers. *J. Geophys. Res. Planets* **2003**, *108*. [CrossRef]
194. Christensen, P.R.; Wyatt, M.B.; Glotch, T.D.; Rogers, A.D.; Anwar, S.; Arvidson, R.E.; Bandfield, J.L.; Blaney, D.L.; Budney, C.; Calvin, W.M. Mineralogy at Meridiani Planum from the Mini-TES experiment on the Opportunity Rover. *Science* **2004**, *306*, 1733–1739. [CrossRef] [PubMed]
195. Greeley, R.; Foing, B.H.; McSween Jr, H.Y.; Neukum, G.; Pinet, P.; van Kan, M.; Werner, S.C.; Williams, D.A.; Zegers, T.E. Fluid lava flows in Gusev crater, Mars. *J. Geophys. Res. Planets* **2005**, *110*. [CrossRef]
196. McSween, H.Y.; Ruff, S.W.; Morris, R.V.; Bell, J.F.; Herkenhoff, K.; Gellert, R.; Stockstill, K.R.; Tornabene, L.L.; Squyres, S.W.; Crisp, J.A.; et al. Alkaline volcanic rocks from the Columbia Hills, Gusev crater, Mars. *J. Geophys. Res. Planets* **2006**, *111*. [CrossRef]
197. McSween, H.Y.; Wyatt, M.B.; Gellert, R.; Bell, J.F., III; Morris, R.V.; Herkenhoff, K.E.; Crumpler, L.S.; Milam, K.A.; Stockstill, K.R.; Tornabene, L.L. Characterization and petrologic interpretation of olivine-rich basalts at Gusev Crater, Mars. *J. Geophys. Res. Planets* **2006**, *111*. [CrossRef]
198. Ming, D.W.; Gellert, R.; Morris, R.V.; Arvidson, R.E.; Brueckner, J.; Clark, B.C.; Cohen, B.A.; d'Uston, C.; Economou, T.; Fleischer, I. Geochemical properties of rocks and soils in Gusev crater, Mars: Results of the Alpha Particle X-ray Spec-trometer from Cumberland Ridge to Home Plate. *J. Geophys. Res. Planets* **2008**, *113*. [CrossRef]
199. Usui, T.; McSween, H.Y., Jr.; Clark, B.C., III. Petrogenesis of high-phosphorous Wishstone Class rocks in Gusev Crater, Mars. *J. Geophys. Res. Planets* **2008**, *113*. [CrossRef]
200. Anderson, R.; Bell, J.F., III. Geologic Mapping and Characterization of Gale Crater and Implications for its Potential as a Mars Science Laboratory Landing Site. *Mars J.* **2010**, *5*, 76–128. [CrossRef]
201. Schwenzer, S.; Abramov, O.; Allen, C.; Clifford, S.; Cockell, C.; Filiberto, J.; Kring, D.; Lasue, J.; McGovern, P.; Newsom, H.; et al. Puncturing Mars: How impact craters interact with the Martian cryosphere. *Earth Planet. Sci. Lett.* **2012**, *335*, 9–17. [CrossRef]

202. Wray, J.J.; Hansen, S.T.; Dufek, J.; Swayze, G.A.; Murchie, S.L.; Seelos, F.P.; Skok, J.R.; Irwin, R.P., III; Ghiorso, M.S. Prolonged magmatic activity on Mars inferred from the detection of felsic rocks. *Nat. Geosci.* **2013**, *6*, 1013–1017. [CrossRef]
203. Farley, K.A.; Malespin, C.; Mahaffy, P.; Grotzinger, J.P.; Vasconcelos, P.M.; Milliken, R.E.; Malin, M.; Edgett, K.S.; Pavlov, A.A.; Hurowitz, J.A.; et al. In situ radiometric and exposure age dating of the Martian surface. *Science* **2014**, *343*, 1247166. [CrossRef]
204. Filiberto, J. Geochemistry of Martian basalts with constraints on magma genesis. *Chem. Geol.* **2017**, *466*, 1–14. [CrossRef]
205. Treiman, A.H. The nakhlite meteorites: Augite-rich igneous rocks from Mars. *Geochemistry* **2005**, *65*, 203–270. [CrossRef]
206. Liu, Y.; Baziotis, I.P.; Asimow, P.D.; Bodnar, R.J.; Taylor, L.A. Mineral chemistry of the Tissint meteorite: Indications of two-stage crystallization in a closed system. *Meteorit. Planet. Sci.* **2016**, *51*, 2293–2315. [CrossRef]
207. Bandfield, J.L.; Rogers, A.D. Olivine dissolution by acidic fluids in Argyre Planitia, Mars: Evidence for a widespread process. *Geology* **2008**, *36*, 579. [CrossRef]
208. Bandfield, J.L.; Rogers, A.D.; Edwards, C.S. The role of aqueous alteration in the formation of martian soils. *Icarus* **2011**, *211*, 157–171. [CrossRef]
209. Salvatore, M.; Mustard, J.; Head, J.; Cooper, R.; Marchant, D.; Wyatt, M. Development of alteration rinds by oxidative weathering processes in Beacon Valley, Antarctica, and implications for Mars. *Geochim. Cosmochim. Acta* **2013**, *115*, 137–161. [CrossRef]
210. Arvidson, R.E.; Squyres, S.W.; Anderson, R.C.; Bell, J.F., III; Blaney, D.; Brueckner, J.; Cabrol, N.A.; Calvin, W.M.; Carr, M.H.; Christensen, P.R. Overview of the spirit Mars exploration rover mission to Gusev Crater: Landing site to Backstay Rock in the Columbia Hills. *J. Geophys. Res. Planets* **2006**, *111*. [CrossRef]
211. Langevin, Y.; Poulet, F.; Bibring, J.-P.; Gondet, B. Sulfates in the North Polar Region of Mars Detected by OMEGA/Mars Express. *Science* **2005**, *307*, 1584–1586. [CrossRef] [PubMed]
212. Fishbaugh, K.E.; Poulet, F.; Chevrier, V.; Langevin, Y.; Bibring, J. On the origin of gypsum in the Mars north polar region. *J. Geophys. Res. Planets* **2007**, *112*. [CrossRef]
213. Horgan, B.H.; Bell, J.F., III; Noe Dobrea, E.Z.; Cloutis, E.A.; Bailey, D.T.; Craig, M.A.; Roach, L.H.; Mustard, J.F. Distribution of hydrated minerals in the north polar region of Mars. *J. Geophys. Res. Planets* **2009**, *114*. [CrossRef]
214. Ruff, S.W.; Farmer, J.D.; Calvin, W.M.; Herkenhoff, K.E.; Johnson, J.R.; Morris, R.V.; Rice, M.S.; Arvidson, R.E.; Bell, J.F., III; Christensen, P.R. Characteristics, distribution, origin, and significance of opaline silica observed by the Spirit rover in Gusev crater, Mars. *J. Geophys. Res. Planets* **2011**, *116*. [CrossRef]
215. Poulet, F.; Omega The Omega Team; Bibring, J.-P.; Mustard, J.F.; Gendrin, A.; Mangold, N.; Langevin, Y.; Arvidson, R.E.; Gondet, B.; Gomez, C. Phyllosilicates on Mars and implications for early Martian climate. *Nature* **2005**, *438*, 623–627. [CrossRef]
216. Bishop, J.L.; Gates, W.P.; Makarewicz, H.D.; McKeown, N.K.; Hiroi, T. Reflectance spectroscopy of beidellites and their importance for Mars. *Clays Clay Miner.* **2011**, *59*, 378–399. [CrossRef]
217. Loizeau, D.; Mangold, N.; Poulet, F.; Ansan, V.; Hauber, E.; Bibring, J.-P.; Gondet, B.; Langevin, Y.; Masson, P.; Neukum, G. Stratigraphy in the Mawrth Vallis region through OMEGA, HRSC color imagery and DTM. *Icarus* **2010**, *205*, 396–418. [CrossRef]
218. Winter, J.D. *Principles of Igneous and Metamorphic Petrology*; Pearson Education: Harlow, UK, 2014.
219. Rosenbauer, R.J.; Bischoff, J.L.; Zierenberg, R.A. The laboratory albitization of mid-ocean ridge basalt. *J. Geol.* **1988**, *96*, 237–244. [CrossRef]
220. Humphris, S.E.; Thompson, G. Hydrothermal alteration of oceanic basalts by seawater. *Geochim. Cosmochim. Acta* **1978**, *42*, 107–125. [CrossRef]
221. Alt, J.C.; Honnorez, J.; Laverne, C.; Emmermann, R. Hydrothermal alteration of a 1 km section through the upper oceanic crust, Deep Sea Drilling Project Hole 504B: Mineralogy, chemistry and evolution of seawater-basalt interactions. *J. Geophys. Res. Solid Earth* **1986**, *91*, 10309–10335. [CrossRef]
222. Neuhoff, P.S.; Fridriksson, T.; Bird, D.K. Zeolite parageneses in the north Atlantic igneous province: Implications for geotectonics and groundwater quality of basaltic crust. *Int. Geol. Rev.* **2000**, *42*, 15–44. [CrossRef]
223. Neuhoff, P.S.; Rogers, K.L.; Stannius, L.S.; Bird, D.K.; Pedersen, A.K. Regional very low-grade metamorphism of basaltic lavas, Disko–Nuussuaq region, West Greenland. *Lithos* **2006**, *92*, 33–54. [CrossRef]
224. Weisenberger, T.; Selbekk, R.S. Multi-stage zeolite facies mineralization in the Hvalfjördur area, Iceland. *Int. J. Earth Sci.* **2009**, *98*, 985–999. [CrossRef]
225. Robert, C.; Goffé, B. Zeolitization of basalts in subaqueous freshwater settings: Field observations and experimental study. *Geochim. Cosmochim. Acta* **1993**, *57*, 3597–3612. [CrossRef]
226. Frost, B.R.; Beard, J.S. On silica activity and serpentinization. *J. Pet.* **2007**, *48*, 1351–1368. [CrossRef]
227. O'Hanley, D.S. *Serpentinites: Records of Tectonic and Petrological History*; Oxford University Press: Oxford, UK, 1966.
228. Frost, B.R.; Beard, J.S.; McCaig, A.; Condliffe, E. The formation of micro-rodingites from IODP Hole U1309D: Key to understanding the process of serpentinization. *J. Pet.* **2008**, *49*, 1579–1588. [CrossRef]
229. Li, X.-P.; Rahn, M.; Bucher, K. Metamorphic processes in rodingites of the Zermatt-Saas ophiolites. *Int. Geol. Rev.* **2004**, *46*, 28–51. [CrossRef]
230. Li, X.; Duan, W.; Zhao, L.; Schertl, H.; Kong, F.; Shi, T.; Zhang, X. Rodingites from the Xigaze ophiolite, southern Tibet–new insights into the processes of rodingitization. *Eur. J. Mineral.* **2017**, *29*, 821–837. [CrossRef]
231. Duan, W.-Y.; Li, X.-P.; Wang, Z.-L.; Chen, S.; Sun, G.-M.; Zhao, L.-Q. Thermodynamic modeling and elemental migration for the early stage of rodingitization: An example from the Xialu massif of the Xigaze ophiolite, southern Tibet. *Geosci. Front.* **2021**, *12*, 101125. [CrossRef]

232. Sleep, N.H.; Meibom, A.; Fridriksson, T.; Coleman, R.G.; Bird, D.K. H_2 -rich fluids from serpentinization: Geochemical and biotic implications. *Proc. Natl. Acad. Sci. USA* **2004**, *101*, 12818–12823. [CrossRef] [PubMed]
233. Sleep, N.H.; Bird, D.K.; Pope, E.C. Serpentinite and the dawn of life. *Philos. Trans. R. Soc. B Biol. Sci.* **2011**, *366*, 2857–2869. [CrossRef] [PubMed]
234. Russell, M.J.; Hall, A.J.; Martin, W. Serpentinization as a source of energy at the origin of life. *Geobiology* **2010**, *8*, 355–371. [CrossRef]
235. Marlow, J.J.; LaRowe, D.; Ehlmann, B.L.; Amend, J.; Orphan, V.J. Bioenergetic and Geobiological Possibilities of Methanotrophy on Mars. In Proceedings of the AGU Fall Meeting Abstracts, San Francisco, CA, USA, 15–19 December 2014.
236. Seto, M.; Noguchi, K.; Van Cappellen, P. Potential for aerobic methanotrophic metabolism on mars. *Astrobiology* **2019**, *19*, 1187–1195. [CrossRef] [PubMed]
237. Russell, M.J.; Ponce, A. Six 'Must-Have' Minerals for Life's Emergence: Olivine, Pyrrhotite, Bridgmanite, Serpentine, Fougerite and Mackinawite. *Life* **2020**, *10*, 291. [CrossRef] [PubMed]
238. Link, L.S.; Jakosky, B.M.; Thyne, G.D. Biological potential of low-temperature aqueous environments on Mars. *Int. J. Astrobiol.* **2005**, *4*, 155–164. [CrossRef]
239. Türke, A.; Nakamura, K.; Bach, W.; Grosch, E.G.; Hazen, R.M.; Konhauser, K.O.; Robbins, L.J.; Pecoits, E.; Peacock, C.; Kappler, A.; et al. Palagonitization of basalt glass in the flanks of mid-ocean ridges: Implications for the bioenergetics of oceanic intracrustal ecosystems. *Astrobiology* **2015**, *15*, 793–803. [CrossRef]
240. Bach, W. Some compositional and kinetic controls on the bioenergetic landscapes in oceanic basement. *Front. Microbiol.* **2016**, *7*, 107. [CrossRef]
241. Semprich, J.; Schwenzer, S.P.; Treiman, A.H.; Filiberto, J. Phase equilibria modeling of low-grade metamorphic Martian rocks. *J. Geophys. Res. Planets* **2019**, *124*, 681–702. [CrossRef]
242. Velde, B.; Vasseur, G. Estimation of the diagenetic smectite to illite transformation in time-temperature space. *Am. Mineral.* **1992**, *77*, 967–976.
243. Berger, G.; Velde, B.; Aigouy, T. Potassium sources and illitization in Texas Gulf Coast shale diagenesis. *J. Sediment. Res.* **1999**, *69*, 151–157. [CrossRef]
244. Lanson, B.; Beaufort, D.; Berger, G.; Bauer, A.; Cassagnabère, A.; Meunier, A. Authigenic kaolin and illitic minerals during burial diagenesis of sandstones: A review. *Clay Miner.* **2002**, *37*, 1–22. [CrossRef]
245. Rasmussen, M.G.; Evans, B.W.; Kuehner, S.M. Low-temperature fayalite, greenalite, and minnesotaite from the Overlook gold deposit, Washington; phase relations in the system FeO-SiO_2-H_2O. *Can. Mineral.* **1998**, *36*, 147–162.
246. Krot, A.N.; Brearley, A.J.; Petaev, M.I.; Kallemeyn, G.W.; Sears, D.W.; Benoit, P.H.; Hutcheon, I.D.; Zolensky, M.E.; Keil, K. Evidence for low-temperature growth of fayalite and hedenbergite in MacAlpine Hills 88107, an ungrouped carbonaceous chondrite related to the CM-CO clan. *Meteorit. Planet. Sci.* **2000**, *35*, 1365–1386. [CrossRef]
247. Daae, F.L.; Økland, I.; Dahle, H.; Jørgensen, S.L.; Thorseth, I.H.; Pedersen, R.B. Microbial life associated with low-temperature alteration of ultramafic rocks in the L eka ophiolite complex. *Geobiology* **2013**, *11*, 318–339. [CrossRef] [PubMed]
248. Miller, H.M.; Matter, J.M.; Kelemen, P.; Ellison, E.T.; Conrad, M.E.; Fierer, N.; Ruchala, T.; Tominaga, M.; Templeton, A.S. Modern water/rock reactions in Oman hyperalkaline peridotite aquifers and implications for microbial habitability. *Geochim. Cosmochim. Acta* **2016**, *179*, 217–241. [CrossRef]
249. Crespo-Medina, M.; Twing, K.I.; Kubo, M.D.Y.; Hoehler, T.M.; Cardace, D.; McCollom, T.; Schrenk, M.O. Insights into environmental controls on microbial communities in a continental serpentinite aquifer using a microcosm-based approach. *Front. Microbiol.* **2014**, *5*, 604. [CrossRef]
250. Rempfert, K.R.; Miller, H.M.; Bompard, N.; Nothaft, D.; Matter, J.M.; Kelemen, P.; Fierer, N.; Templeton, A.S. Ge-ological and geochemical controls on subsurface microbial life in the Samail Ophiolite, Oman. *Front. Microbiol.* **2017**, *8*, 56. [CrossRef]
251. Twing, K.I.; Brazelton, W.J.; Kubo, M.D.Y.; Hyer, A.J.; Cardace, D.; Hoehler, T.M.; McCollom, T.M.; Schrenk, M.O. Serpentinization-Influenced Groundwater Harbors Extremely Low Diversity Microbial Communities Adapted to High pH. *Front. Microbiol.* **2017**, *8*, 308. [CrossRef]
252. Newman, S.A.; Lincoln, S.A.; O'Reilly, S.; Liu, X.; Shock, E.L.; Kelemen, P.B.; Summons, R.E. Lipid Biomarker Record of the Serpentinite-Hosted Ecosystem of the Samail Ophiolite, Oman and Implications for the Search for Biosignatures on Mars. *Astrobiology* **2020**, *20*, 830–845. [CrossRef]
253. Seyler, L.M.; Brazelton, W.J.; McLean, C.; Putman, L.I.; Hyer, A.; Kubo, M.D.Y.; Hoehler, T.; Cardace, D.; Schrenk, M.O. Carbon Assimilation Strategies in Ultrabasic Groundwater: Clues from the Integrated Study of a Serpentinization-Influenced Aquifer. *mSystems* **2020**, *5*. [CrossRef] [PubMed]
254. Barnes, I.; LaMarche Jr, V.C.; Himmelberg, G. Geochemical evidence of present-day serpentinization. *Science* **1967**, *156*, 830–832. [CrossRef] [PubMed]
255. Ortiz, E.; Tominaga, M.; Cardace, D.; Schrenk, M.O.; Hoehler, T.M.; Kubo, M.D.; Rucker, D.F. Geophysical Characterization of Serpentinite Hosted Hydrogeology at the McLaughlin Natural Reserve, Coast Range Ophiolite. *Geochem. Geophys. Geosyst.* **2018**, *19*, 114–131. [CrossRef]
256. Paukert, A.N.; Matter, J.M.; Kelemen, P.B.; Shock, E.L.; Havig, J.R. Reaction path modeling of enhanced in situ CO_2 mineralization for carbon sequestration in the peridotite of the Samail Ophiolite, Sultanate of Oman. *Chem. Geol.* **2012**, *330–331*, 86–100. [CrossRef]

257. Boulart, C.; Chavagnac, V.; Monnin, C.; Delacour, A.; Ceuleneer, G.; Hoareau, G. Differences in gas venting from ultramafic-hosted warm springs: The example of Oman and Voltri ophiolites. *Ofioliti* **2013**, *38*, 143–156.
258. Chavagnac, V.; Ceuleneer, G.; Monnin, C.; Lansac, B.; Hoareau, G.; Boulart, C. Mineralogical assemblages forming at hyperalkaline warm springs hosted on ultramafic rocks: A case study of Oman and Ligurian ophiolites. *Geochem. Geophys. Geosyst.* **2013**, *14*, 2474–2495. [CrossRef]
259. Brazelton, W.J.; Morrill, P.L.; Szponar, N.; Schrenk, M.O. Bacterial communities associated with subsurface geo-chemical processes in continental serpentinite springs. *Appl. Environ. Microbiol.* **2013**, *79*, 3906–3916. [CrossRef]
260. Szponar, N.; Brazelton, W.J.; Schrenk, M.O.; Bower, D.M.; Steele, A.; Morrill, P.L. Geochemistry of a continental site of serpentinization, the Tablelands Ophiolite, Gros Morne National Park: A Mars analogue. *Icarus* **2013**, *224*, 286–296. [CrossRef]
261. Sánchez-Murillo, R.; Gazel, E.; Schwarzenbach, E.M.; Crespo-Medina, M.; Schrenk, M.O.; Boll, J.; Gill, B.C. Geochemical evidence for active tropical serpentinization in the Santa Elena Ophiolite, Costa Rica: An analog of a humid early Earth. *Geochem. Geophys. Geosyst.* **2014**, *15*, 1783–1800. [CrossRef]
262. Fernández-Remolar, D.C.; Prieto-Ballesteros, O.; Rodríguez, N.; Gómez, F.; Amils, R.; Gómez-Elvira, J.; Stoker, C.R. Underground habitats in the Río Tinto basin: A model for subsurface life habitats on Mars. *Astrobiology* **2008**, *8*, 1023–1047. [CrossRef]
263. Etiope, G.; Vance, S.; Christensen, L.E.; Marques, J.M.; da Costa, I.R. Methane in serpentinized ultramafic rocks in mainland Portugal. *Mar. Pet. Geol.* **2013**, *45*, 12–16. [CrossRef]
264. Etiope, G.; Vadillo, I.; Whiticar, M.; Marques, J.; Carreira, P.; Tiago, I.; Benavente, J.; Jiménez, P.; Urresti, B. Abiotic methane seepage in the Ronda peridotite massif, southern Spain. *Appl. Geochem.* **2016**, *66*, 101–113. [CrossRef]
265. Purkamo, L.; Bomberg, M.; Nyyssönen, M.; Kukkonen, I.; Ahonen, L.; Itävaara, M. Heterotrophic communities sup-plied by ancient organic carbon predominate in deep Fennoscandian bedrock fluids. *Microb. Ecol.* **2015**, *69*, 319–332. [CrossRef] [PubMed]
266. Parkes, R.J.; Cragg, B.A.; Bale, S.J.; Getlifff, J.M.; Goodman, K.; Rochelle, P.A.; Fry, J.C.; Weightman, A.J.; Harvey, S.M. Deep bacterial biosphere in Pacific Ocean sediments. *Nature* **1994**, *371*, 410–413. [CrossRef]
267. D'Hondt, S.; Rutherford, S.; Spivack, A.J. Metabolic activity of subsurface life in deep-sea sediments. *Science* **2002**, *295*, 2067–2070. [CrossRef]
268. Van Dover, C.L.; Fry, B. Microorganisms as food resources at deep-sea hydrothermal vents. *Limnol. Oceanogr.* **1994**, *39*, 51–57. [CrossRef]
269. Proskurowski, G.; Lilley, M.D.; Seewald, J.S.; Früh-Green, G.L.; Olson, E.J.; Lupton, J.E.; Sylva, S.P.; Kelley, D.S. Abiogenic hydrocarbon production at Lost City hydrothermal field. *Science* **2008**, *319*, 604–607. [CrossRef]
270. Stevens, T.O.; McKinley, J.P. Lithoautotrophic microbial ecosystems in deep basalt aquifers. *Science* **1995**, *270*, 450–455. [CrossRef]
271. Lang, S.Q.; Früh-Green, G.L.; Kelley, D.S.; Lilley, M.D.; Proskurowski, G.; Reeves, E.P. H_2/CH_4 ratios cannot reliably distinguish abiotic vs. biotic methane in natural hydrothermal systems. *Proc. Natl. Acad. Sci. USA* **2012**, *109*, E3210. [CrossRef]
272. Schrenk, M.O.; Brazelton, W.J.; Lang, S.Q. Serpentinization, carbon, and deep life. *Rev. Miner. Geochem.* **2013**, *75*, 575–606. [CrossRef]
273. Dick, G.J.; Anantharaman, K.; Baker, B.J.; Li, M.; Reed, D.C.; Sheik, C.S. The microbiology of deep-sea hydrothermal vent plumes: Ecological and biogeographic linkages to seafloor and water column habitats. *Front. Microbiol.* **2013**, *4*, 124. [CrossRef] [PubMed]
274. Brazelton, W.J.; Schrenk, M.O.; Kelley, D.S.; Baross, J.A. Methane- and Sulfur-Metabolizing Microbial Communities Dominate the Lost City Hydrothermal Field Ecosystem. *Appl. Environ. Microbiol.* **2006**, *72*, 6257–6270. [CrossRef] [PubMed]
275. Brazelton, W.J.; Mehta, M.P.; Kelley, D.S.; Handelsman, J. Physiological differentiation within a single-species biofilm fueled by serpentinization. *mBio* **2011**, *2*, 1–9. [CrossRef] [PubMed]
276. Coskun, K.; Vuillemin, A.; Schubotz, F.; Klein, F.; Sichel, S.E.; Eisenreich, W.; Orsi, W.D. Quantifying the effects of hydrogen on carbon assimilation in a seafloor microbial community associated with ultramafic rocks. *ISME J.* **2021**, *16*, 257–271. [CrossRef] [PubMed]
277. Altshuler, I.; Goordial, J.; Whyte, L.G. Microbial life in permafrost. *Psychrophiles Biodivers. Biotechnol.* **2017**, 153–179.
278. Tuorto, S.J.; Darias, P.; McGuinness, L.R.; Panikov, N.; Zhang, T.; Häggblom, M.M.; Kerkhof, L.J. Bacterial genome replication at subzero temperatures in permafrost. *ISME J.* **2014**, *8*, 139–149. [CrossRef] [PubMed]
279. He, R.; Wooller, M.J.; Pohlman, J.W.; Quensen, J.; Tiedje, J.M.; Leigh, M.B. Shifts in identity and activity of metha-notrophs in arctic lake sediments in response to temperature changes. *Appl. Environ. Microbiol.* **2012**, *78*, 4715–4723. [CrossRef]
280. Froelich, P.; Klinkhammer, G.P.; Bender, M.L.; Luedtke, N.A.; Heath, G.R.; Cullen, D.; Dauphin, P.; Hammond, D.; Hartman, B.; Maynard, V. Early oxidation of organic matter in pelagic sediments of the eastern equatorial Atlantic: Suboxic diagenesis. *Geochim. Cosmochim. Acta* **1979**, *43*, 1075–1090. [CrossRef]
281. Coleman, D.C.; Reid, C.; Cole, C.V. Biological strategies of nutrient cycling in soil systems. In *Advances in Ecological Research*; Elsevier: Amsterdam, The Netherlands, 1983; pp. 1–55.
282. Friedmann, E.I. Endolithic microorganisms in the Antarctic cold desert. *Science* **1982**, *215*, 1045–1053. [CrossRef]
283. Balkwill, D.L.; Ghiorse, W.C. Characterization of subsurface bacteria associated with two shallow aquifers in Oklahoma. *Appl. Environ. Microbiol.* **1985**, *50*, 580–588. [CrossRef]
284. Federle, T.W.; Dobbins, D.C.; Thornton-Manning, J.R.; Jones, D.D. Microbial biomass, activity, and community structure in subsurface soils. *Groundwater* **1986**, *24*, 365–374. [CrossRef]
285. Wong, F.K.Y.; Lau, M.C.Y.; Lacap, D.C.; Aitchison, J.C.; Cowan, D.A.; Pointing, S.B. Endolithic microbial colonization of limestone in a high-altitude arid environment. *Microb. Ecol.* **2010**, *59*, 689–699. [CrossRef] [PubMed]

286. Ji, M.; Greening, C.; Vanwonterghem, I.; Carere, C.R.; Bay, S.K.; Steen, J.A.; Montgomery, K.; Lines, T.; Beardall, J.; van Dorst, J.; et al. Atmospheric trace gases support primary production in Antarctic desert surface soil. *Nature* **2017**, *552*, 400–403. [CrossRef] [PubMed]
287. Lau, M.C.Y.; Stackhouse, B.T.; Layton, A.C.; Chauhan, A.; Vishnivetskaya, T.A.; Chourey, K.; Ronholm, J.; Mykytczuk, N.C.S.; Bennett, P.C.; Lamarche-Gagnon, G.; et al. An active atmospheric methane sink in high Arctic mineral cryosols. *ISME J.* **2015**, *9*, 1880–1891. [CrossRef] [PubMed]
288. van Lingen, H.J.; Edwards, J.E.; Vaidya, J.D.; van Gastelen, S.; Saccenti, E.; Bogert, B.v.D.; Bannink, A.; Smidt, H.; Plugge, C.M.; Dijkstra, J. Diurnal dynamics of gaseous and dissolved metabolites and microbiota composition in the bovine rumen. *Front. Microbiol.* **2017**, *8*, 425. [CrossRef] [PubMed]
289. Kelley, D.S.; Karson, J.A.; Früh-Green, G.L.; Yoerger, D.R.; Shank, T.M.; Butterfield, D.A.; Hayes, J.M.; Schrenk, M.O.; Olson, E.J.; Proskurowski, G.; et al. A Serpentinite-Hosted Ecosystem: The Lost City Hydrothermal Field. *Science* **2005**, *307*, 1428–1434. [CrossRef]
290. Roussel, E.G.; Konn, C.; Charlou, J.-L.; Donval, J.-P.; Fouquet, Y.; Querellou, J.; Prieur, D.; Bonavita, M.-A.C. Comparison of microbial communities associated with three Atlantic ultramafic hydrothermal systems. *FEMS Microbiol. Ecol.* **2011**, *77*, 647–665. [CrossRef] [PubMed]
291. Woycheese, K.M.; Meyer-Dombard, D.R.; Cardace, D.; Argayosa, A.M.; Arcilla, C.A. Out of the dark: Transitional subsurface-to-surface microbial diversity in a terrestrial serpentinizing seep (Manleluag, Pangasinan, the Philippines). *Front. Microbiol.* **2015**, *6*, 44. [CrossRef]
292. Blank, J.; Green, S.; Blake, D.; Valley, J.; Kita, N.; Treiman, A.; Dobson, P. An alkaline spring system within the Del Puerto Ophiolite (California, USA): A Mars analog site. *Planet. Space Sci.* **2009**, *57*, 533–540. [CrossRef]
293. Mottl, M.J.; Komor, S.C.; Fryer, P.; Moyer, C.L. Deep-slab fluids fuel extremophilic *Archaea* on a Mariana forearc serpentinite mud volcano: Ocean Drilling Program Leg 195. *Geochem. Geophys. Geosyst.* **2003**, *4*. [CrossRef]
294. Grimm, R.E.; Harrison, K.P.; Stillman, D.E.; Kirchoff, M.R. On the secular retention of ground water and ice on Mars. *J. Geophys. Res. Planets* **2017**, *122*, 94–109. [CrossRef]
295. Manga, M.; Wright, V. No Cryosphere-Confined Aquifer Below InSight on Mars. *Geophys. Res. Lett.* **2021**, *48*, e2021GL093127. [CrossRef]
296. Michalski, J.R.; Goudge, T.A.; Crowe, S.A.; Cuadros, J.; Mustard, J.F.; Johnson, S.S. Geological diversity and microbiological potential of lakes on Mars. *Nat. Astron.* **2022**, *6*, 1133–1141. [CrossRef]
297. Stillman, D.E.; Michaels, T.I.; Grimm, R.E. Characteristics of the numerous and widespread recurring slope lineae (RSL) in Valles Marineris, Mars. *Icarus* **2017**, *285*, 195–210. [CrossRef]
298. Mitchell, J.L.; Christensen, P.R. Recurring slope lineae and chlorides on the surface of Mars. *J. Geophys. Res. Planets* **2016**, *121*, 1411–1428. [CrossRef]
299. Colman, D.R.; Kraus, E.A.; Thieringer, P.H.; Rempfert, K.; Templeton, A.S.; Spear, J.R.; Boyd, E.S. Deep-branching acetogens in serpentinized subsurface fluids of Oman. *Proc. Natl. Acad. Sci. USA* **2022**, *119*, e2206845119. [CrossRef]
300. Suzuki, S.; Nealson, K.H.; Ishii, S. Genomic and in-situ transcriptomic characterization of the candidate phylum NPL-UPL2 from highly alkaline highly reducing serpentinized groundwater. *Front. Microbiol.* **2018**, *9*, 3141. [CrossRef]
301. Merino, N.; Kawai, M.; Boyd, E.S.; Colman, D.R.; McGlynn, S.E.; Nealson, K.H.; Kurokawa, K.; Hongoh, Y. Single-cell genomics of novel actinobacteria with the Wood–Ljungdahl pathway discovered in a serpentinizing system. *Front. Microbiol.* **2020**, *11*, 1031. [CrossRef]
302. Barber, D.J.; Scott, E.R.D. Shock and thermal history of Martian meteorite Allan Hills 84001 from transmission electron microscopy. *Meteorit. Planet. Sci.* **2006**, *41*, 643–662. [CrossRef]
303. Lorand, J.-P.; Hewins, R.; Humayun, M.; Remusat, L.; Zanda, B.; La, C.; Pont, S. Chalcophile-siderophile element systematics of hydrothermal pyrite from martian regolith breccia NWA 7533. *Geochim. Cosmochim. Acta* **2018**, *241*, 134–149. [CrossRef]
304. Pascuzzo, A.C.; Mustard, J.F.; Kremer, C.H.; Ebinger, E. The formation of irregular polygonal ridge networks, Nili Fossae, Mars: Implications for extensive subsurface channelized fluid flow in the Noachian. *Icarus* **2019**, *319*, 852–868. [CrossRef]
305. Bridges, J.C.; Schwenzer, S.P.; Leveille, R.; Westall, F.; Wiens, R.C.; Mangold, N.; Bristow, T.; Edwards, P.; Berger, G. Diagenesis and clay mineral formation at Gale Crater, Mars. *J. Geophys. Res. Planets* **2015**, *120*, 1–19. [CrossRef] [PubMed]
306. McSween, H.Y., Jr.; Labotka, T.C.; Viviano-Beck, C.E. Metamorphism in the Martian crust. *Meteorit. Planet. Sci.* **2015**, *50*, 590–603. [CrossRef]
307. Scheller, E.L.; Hollis, J.R.; Cardarelli, E.L.; Steele, A.; Beegle, L.W.; Bhartia, R.; Conrad, P.; Uckert, K.; Sharma, S.; Ehlmann, B.L.; et al. Aqueous alteration processes in Jezero crater, Mars—Implications for organic geochemistry. *Science* **2022**, *378*, 1105–1110. [CrossRef] [PubMed]
308. Steele, A.; Benning, L.G.; Wirth, R.; Schreiber, A.; Araki, T.; McCubbin, F.M.; Fries, M.D.; Nittler, L.R.; Wang, J.; Hallis, L.J.; et al. Organic synthesis associated with serpentinization and carbonation on early Mars. *Science* **2022**, *375*, 172–177. [CrossRef] [PubMed]
309. Wright, I.P.; Grady, M.M.; Pillinger, C.T. Organic materials in a martian meteorite. *Nature* **1989**, *340*, 220–222. [CrossRef]
310. McKay, D.S.; Gibson Jr, E.K.; Thomas-Keprta, K.L.; Vali, H.; Romanek, C.S.; Clemett, S.J.; Chillier, X.D.; Maechling, C.R.; Zare, R.N. Search for past life on Mars: Possible relic biogenic activity in Martian meteorite ALH84001. *Science* **1996**, *273*, 924–930. [CrossRef]

311. Bada, J.L.; Glavin, D.P.; McDonald, G.D.; Becker, L. A search for endogenous amino acids in Martian meteorite ALH84001. *Science* **1998**, *279*, 362–365. [CrossRef]
312. Becker, L.; Popp, B.; Rust, T.; Bada, J.L. The origin of organic matter in the Martian meteorite ALH84001. *Adv. Space Res.* **1999**, *24*, 477–488. [CrossRef]
313. Zolotov, M.; Shock, E. Abiotic synthesis of polycyclic aromatic hydrocarbons on Mars. *J. Geophys. Res. Atmos.* **1999**, *104*, 14033–14049. [CrossRef]
314. Zolotov, M.Y.; Shock, E.L. An abiotic origin for hydrocarbons in the Allan Hills 84001 martian meteorite through cooling of magmatic and impact-generated gases. *Meteorit. Planet. Sci.* **2000**, *35*, 629–638. [CrossRef] [PubMed]
315. Gibson Jr, E.K.; McKay, D.S.; Thomas-Keprta, K.L.; Wentworth, S.J.; Westall, F.; Steele, A.; Romanek, C.S.; Bell, M.S.; Toporski, J. Life on Mars: Evaluation of the evidence within Martian meteorites ALH84001, Nakhla, and Shergotty. *Precambrian Res.* **2001**, *106*, 15–34. [CrossRef]
316. Carr, M.H.; Head, J.W. Geologic history of Mars. *Earth Planet. Sci. Lett.* **2010**, *294*, 185–203. [CrossRef]
317. Hauber, E.; Brož, P.; Jagert, F.; Jodłowski, P.; Platz, T. Very recent and wide-spread basaltic volcanism on Mars. *Geophys. Res. Lett.* **2011**, *38*, L10201. [CrossRef]
318. Krishnan, V.; Kumar, P.S. Long-Lived and Continual Volcanic Eruptions, Tectonic Activity, Pit Chains Formation, and Boulder Avalanches in Northern Tharsis Region: Implications for Late Amazonian Geodynamics and Seismo-Tectonic Processes on Mars. *J. Geophys. Res. Planets* **2023**, *128*, e2022JE007511. [CrossRef]
319. Ahmad, A.; Patel, R.; Deka, B.; Nagori, R.; Arya, A.; Nair, A.M. Occurrence of secondary minerals at Tharsis Montes of Mars: A critical assessment. *Icarus* **2022**, *378*, 114953. [CrossRef]
320. Melosh, H.J.; Vickery, A.M. Impact erosion of the primordial atmosphere of Mars. *Nature* **1989**, *338*, 487–489. [CrossRef]
321. Abramov, O.; Kring, D.A. Impact-induced hydrothermal activity on early Mars. *J. Geophys. Res. Planets* **2005**, *110*. [CrossRef]
322. Joeleht, A.; Kirsimäe, K.; Plado, J.; Versh, E.; Ivanov, B. Cooling of the Kärdla impact crater: II. Impact and geo-thermal modeling. *Meteorit. Planet. Sci.* **2005**, *40*, 21–33. [CrossRef]
323. Ames, D.E.; Watkinson, D.H.; Parrish, R.R. Dating of a regional hydrothermal system induced by the 1850 Ma Sudbury impact event. *Geology* **1998**, *26*, 447–450. [CrossRef]
324. Abramov, O.; Kring, D.A. Numerical modeling of impact-induced hydrothermal activity at the Chicxulub crater. *Meteorit. Planet. Sci.* **2007**, *42*, 93–112. [CrossRef]
325. Grant, J.A.; Irwin, R.P., III; Grotzinger, J.P.; Milliken, R.E.; Tornabene, L.L.; McEwen, A.S.; Weitz, C.M.; Squyres, S.W.; Glotch, T.S.; Thomson, B.J. HiRISE imaging of impact megabreccia and sub-meter aqueous strata in Holden Crater, Mars. *Geology* **2008**, *36*, 195–198. [CrossRef]
326. Marzo, G.A.; Davila, A.F.; Tornabene, L.L.; Dohm, J.M.; Fairén, A.G.; Gross, C.; Kneissl, T.; Bishop, J.L.; Roush, T.L.; McKay, C.P. Evidence for Hesperian impact-induced hydrothermalism on Mars. *Icarus* **2010**, *208*, 667–683. [CrossRef]
327. Turner, S.M.R.; Bridges, J.C.; Grebby, S.; Ehlmann, B.L. Hydrothermal activity recorded in post Noachian-aged impact craters on Mars. *J. Geophys. Res. Planets* **2016**, *121*, 608–625. [CrossRef]
328. Robbins, S.J.; Hynek, B.M. A new global database of Mars impact craters≥ 1 km: 1. Database creation, properties, and parameters. *J. Geophys. Res. Planets* **2012**, *117*. [CrossRef]
329. Rathbun, J.A.; Squyres, S.W. Hydrothermal systems associated with Martian impact craters. *Icarus* **2002**, *157*, 362–372. [CrossRef]
330. Cockell, C.S.; Voytek, M.A.; Gronstal, A.L.; Finster, K.; Kirshtein, J.D.; Howard, K.; Reitner, J.; Gohn, G.S.; Sanford, W.E.; Horton, J.W.; et al. Impact disruption and recovery of the deep subsurface biosphere. *Astrobiology* **2012**, *12*, 231–246. [CrossRef] [PubMed]
331. Ojha, L.; Karunatillake, S.; Karimi, S.; Buffo, J. Amagmatic hydrothermal systems on Mars from radiogenic heat. *Nat. Commun.* **2021**, *12*, 1–11. [CrossRef] [PubMed]
332. Michalski, J.R.; Dobrea, E.Z.N.; Niles, P.B.; Cuadros, J. Ancient hydrothermal seafloor deposits in Eridania basin on Mars. *Nat. Commun.* **2017**, *8*, 15978. [CrossRef]
333. Stephan, T.; Jessberger, E.K.; Heiss, C.H.; Rost, D. TOF-SIMS analysis of polycyclic aromatic hydrocarbons in Allan Hills 84001. *Meteorit. Planet. Sci.* **2003**, *38*, 109–116. [CrossRef]
334. Eigenbrode, J.L.; Summons, R.E.; Steele, A.; Freissinet, C.; Millan, M.; Navarro-González, R.; Sutter, B.; McAdam, A.C.; Franz, H.B.; Glavin, D.P.; et al. Organic matter preserved in 3-billion-year-old mudstones at Gale crater, Mars. *Science* **2018**, *360*, 1096–1101. [CrossRef] [PubMed]
335. Mckay, C.P.; Stoker, C.R. Could the early environment of Mars have supported the development of life? *Earth Space* **1990**, *2*, 10–12. [PubMed]
336. McKay, C.P. An origin of life on Mars. *Cold Spring Harb. Perspect. Biol.* **2010**, *2*, a003509. [CrossRef] [PubMed]
337. McKay, C.P.; Stoker, C.R.; Glass, B.J.; Davé, A.I.; Davila, A.F.; Heldmann, J.L.; Marinova, M.M.; Fairen, A.G.; Quinn, R.C.; Zacny, K.A.; et al. The Icebreaker Life Mission to Mars: A search for biomolecular evidence for life. *Astrobiology* **2013**, *13*, 334–353. [CrossRef] [PubMed]
338. McKay, C.P. Past, present, and future life on Mars. *Gravit. Space Biol. Bull. Publ. Am. Soc. Gravit. Space Biol.* **1998**, *11*, 41–50.
339. Ingersoll, A.P. Mars: Occurrence of Liquid Water. *Science* **1970**, *168*, 972–973. [CrossRef]
340. McKay, C.P.; Davis, W.L. Duration of liquid water habitats on early Mars. *Icarus* **1991**, *90*, 214–221. [CrossRef]
341. Haberle, R.M.; McKay, C.P.; Schaeffer, J.; Cabrol, N.A.; Grin, E.A.; Zent, A.P.; Quinn, R. On the possibility of liquid water on present-day Mars. *J. Geophys. Res. Planets* **2001**, *106*, 23317–23326. [CrossRef]

342. Hecht, M. Metastability of Liquid Water on Mars. *Icarus* **2002**, *156*, 373–386. [CrossRef]
343. Wray, J.J. Contemporary liquid water on Mars? *Annu. Rev. Earth Planet. Sci.* **2021**, *49*, 141–171. [CrossRef]
344. Mitchell, K.L.; Wilson, L. Mars: A geologically active planet. *Astron. Geophys.* **2003**, *44*, 4.16–4.20. [CrossRef]
345. Viviano-Beck, C.; Murchie, S.; Beck, A.; Dohm, J. Compositional and structural constraints on the geologic history of eastern Tharsis Rise, Mars. *Icarus* **2017**, *284*, 43–58. [CrossRef]